INFORMATION TO USERS

This manuscript has been reproduced from the microfilm master. UMI films the text directly from the original or copy submitted. Thus, some thesis and dissertation copies are in typewriter face, while others may be from any type of computer printer.

The quality of this reproduction is dependent upon the quality of the copy submitted. Broken or indistinct print, colored or poor quality illustrations and photographs, print bleedthrough, substandard margins, and improper alignment can adversely affect reproduction.

In the unlikely event that the author did not send UMI a complete manuscript and there are missing pages, these will be noted. Also, if unauthorized copyright material had to be removed, a note will indicate the deletion.

Oversize materials (e.g., maps, drawings, charts) are reproduced by sectioning the original, beginning at the upper left-hand corner and continuing from left to right in equal sections with small overlaps.

Photographs included in the original manuscript have been reproduced xerographically in this copy. Higher quality 6" x 9" black and white photographic prints are available for any photographs or illustrations appearing in this copy for an additional charge. Contact UMI directly to order.

Bell & Howell Information and Learning
300 North Zeeb Road, Ann Arbor, MI 48106-1346 USA

UMI®
800-521-0600

SUPERDEFORMATION: A TOOL TO STUDY FUSION-EVAPORATION REACTIONS

By

JOHN MATTI NIEMINEN, B.SC., M.SC.

A Thesis

Submitted to the School of Graduate Studies

in Partial Fulfillment of the Requirements

for the Degree

Doctor of Philosophy.

McMaster University

SD: A TOOL TO STUDY FUSION-EVAPORATION REACTIONS

DOCTOR OF PHILOSOPHY (1998)
(Physics)

McMaster University
Hamilton, Ontario

TITLE: Superdeformation:
A Tool to Study Fusion-Evaporation Reactions

AUTHOR: John M. Nieminen, B.Sc., M.Sc. (Laurentian University)

SUPERVISOR: Dr. S. Flibotte

NUMBER OF PAGES: xi, 94

Abstract

In recent experiments it has been observed that some discrete superdeformed bands in the mass $A \sim 150$ region are more strongly populated when mass-symmetric target-projectile combinations are used. It is proposed in this Thesis that these population differences result from a modification of the compound-nucleus angular-momentum distribution due to the presence of low-lying vibrational states in the target/projectile nuclei.

Testing this hypothesis, for reactions leading to the population of superdeformed bands in the mass $A \sim 150$ region, is difficult because the fission process begins to compete with the formation of evaporation residues. This, however, is not a problem in the mass $A \sim 130$ region and a study of the nucleus ^{135}Nd was therefore undertaken with the reactions ^{74}Ge+^{64}Ni and ^{26}Mg+^{112}Cd. Angular-momentum distributions, when coupling to vibrational states was not considered, and excitation energies of the compound nucleus ^{138}Nd were closely matched for the two reactions. The ^{74}Ge-induced mass-symmetric reaction was found to preferentially populate high-spin states, including superdeformed states in ^{135}Nd. This is the first report of such an effect in the mass $A \sim 130$ region and the first time that such measurements have been made as a function of spin for individual superdeformed states. Statistical-model calculations were shown to be in agreement with the present observations provided coupled-channel effects were taken into account.

To learn more about population mechanisms in the mass $A \sim 150$ region, a study of superdeformed band population at very high angular momenta was initiated with the reactions ^{76}Ge+^{76}Ge and ^{28}Si+^{124}Sn. Both reactions formed the compound nucleus ^{152}Gd at an excitation energy of 87 MeV. Relative to normally deformed

states, the yrast superdeformed band in the residual nucleus ^{147}Gd was found to be populated 4.6 ± 0.2 times more strongly for the mass-symmetric reaction compared to the mass-asymmetric reaction. Such a large difference in the population was not expected. Furthermore, the superdeformed continuum feeding the yrast superdeformed states in ^{147}Gd was found to be at least 12 times stronger, relative to the population of the channel, for the mass-symmetric reaction. Statistical-model calculations, similar to those preformed in the mass $A \sim 130$ region study, could not reproduce the experimental results. Experiments like the one presented in this Thesis may provide valuable information about the fission barrier at very high angular momenta.

Acknowledgements

"I'd like to say thank you on behalf of the group and ourselves, and I hope we passed the audition."

John Lennon (1940-1980)
The Beatles, Get Back [1]

I'd like to say thank you to my friend Dr. Stéphane Flibotte, the supervisor of this Thesis, for the insight, knowledge, and great sense of humour that he has shared with me over the past few years. I am grateful to the committee members, Dr. James C. Waddington and Dr. Randall S. Dumont, for their helpful suggestions and guidance throughout this work. Thanks are also extended to all the members of the 8π group and to all the other collaborators listed in references [2, 3, 4].

The completion of this work could not have come about without the constant support of my friends and family and I appreciate everyone of them. Most importantly, I wish to express my deepest gratitude to my wife Clare and our rabbit Chelsea for their undying love. This Thesis is dedicated to them.

Contents

List of Figures

List of Tables

Chapter 1

Introduction

"You are also asking me questions and I hear you,
I answer that I cannot answer, you must find out for yourself."

Walt Whitman (1819-1892)
Song of Myself [5]

Nuclear angular momentum has been a topic of great interest and growth over the past few decades. The angular momentum of a nucleus can be thought of as arising from two main components. The first of these is the overall motion of the nucleus and the second is the orbital and spin angular momenta of its individual nucleons. The interaction between the collective and single-particle degrees of freedom makes nuclei fascinating systems to study. By studying nuclei that exhibit high angular momenta an even greater knowledge of the collective and single-particle motions involved in defining their rotational structures has been gained. On equal footing, though perhaps of greater interest, has been the discovery of new phenomena; one of the most well known being that of superdeformation.

As the nucleus takes on large values of angular momentum it can become energetically favourable for it to exhibit larger deformations. This is especially true in mass regions where shell effects can help to stabilize these deformed shapes. Nu-

clei with superdeformed shapes, having an axis ratio of approximately 2:1:1 (cigar shaped), were first observed, at low spin, in fission isomers in the actinide region [6]. Discrete superdeformed bands were later observed in the mass $A \sim 130$ [7], $A \sim 150$ [8], and $A \sim 190$ [9] regions. More recently superdeformed bands have been found in the mass $A \sim 80$ [10] and $A \sim 60$ [11] regions. In all, approximately 200 superdeformed structures (bands) have been documented [12] and much has been learned about the relationships between these bands as well as their individual configurations and properties.

The main focus of this Thesis is to use superdeformation as a "tool" to study fusion-evaporation reactions by measuring superdeformed band population. Given what is known about superdeformed bands, in particular their occurrence at high spin and their well defined structures, the intent now is to use them as probes to study compound nucleus formation followed by particle evaporation. In particular, superdeformed band population is examined in the mass $A \sim 130$ and $A \sim 150$ regions and ambiguities in existing interpretations of the processes governing fusion-evaporation reactions are scrutinized.

The work in this Thesis falls into two main sections. The first section deals with fundamental concepts needed for a complete understanding of the material presented within the body of the work. Chapter 2 gives a brief introduction to some of the terminology used in the field of high-spin physics and chapter 3 discusses experimental techniques used in the acquisition and analysis of data. Computer codes used in the modelling of observed phenomena are described in chapter 4. The second part of this Thesis concerns experiments performed by the author and collaborators. The phenomenon of superdeformation is looked at in detail in chapter 5 with the discovery of a new superdeformed band in the nucleus ^{147}Tb being unveiled. In chapter 6 im-

portant questions about the fusion process, for mass-symmetric and mass-asymmetric reactions leading to the same compound system, are addressed in a comparative study of high-spin states in the residual nucleus ^{135}Nd. Superdeformed band population at extreme angular momenta is then examined in chapter 7. More precisely, an in depth study of the feeding process of the yrast superdeformed band in the residual nucleus ^{147}Gd is presented. Chapter 8 presents a brief summary of this Thesis as a whole.

Chapter 2

Excitations of the Nucleus

" 'The rules are tricky, but they are a much more efficient way of getting the answer than by counting beans.' "

Richard P. Feynman (1918-1988)
QED [13]

When a nucleus is produced in a nuclear reaction various modes of excitation can occur. If individual nucleons are raised to orbitals of higher energy than that of the ground-state configuration then single-particle excitations are said to have occurred. When several nucleons are involved in the excitation then the motion of the group may be collective and the nucleus may exhibit rotational and/or vibrational motions. The aim of this chapter is to introduce basic concepts of nuclear excitation, beginning with an overview of collective motions of the nucleus. Brief descriptions of the Nilsson model (single-particle model for deformed nuclei) and the cranked shell model are then given.

2.1 Nuclear Shapes

One of the simplest models of the nucleus is that of an incompressible liquid drop whose shape can be parameterized by expanding the radius $R(\theta, \phi)$ as

$$R(\theta, \phi) = R_0 \left(1 + \sum_{\lambda=0}^{\infty} \sum_{\mu=-\lambda}^{\lambda} \alpha_{\lambda\mu} Y_{\lambda\mu}(\theta, \phi) \right) \tag{2.1}$$

where $Y_{\lambda\mu}(\theta, \phi)$ are the spherical harmonics, R_0 is the radius of a sphere which has the same volume as $R(\theta, \phi)$, and $\alpha_{\lambda\mu}$ are deformation parameters. The parameters α_{00} and $\alpha_{1\mu}$ are taken to be zero since they represent cases where changes in volume and displacement of the center of mass occur, respectively, and the five $\alpha_{2\mu}$ parameters are commonly expressed in Hill-Wheeler coordinates [14]:

$$\begin{aligned} \alpha_{20} &= \beta_2 \cos\gamma \\ \alpha_{2\pm1} &= 0 \\ \alpha_{2\pm2} &= \frac{1}{\sqrt{2}} \beta_2 \sin\gamma \end{aligned} \tag{2.2}$$

Figure 2.1 shows special cases of deformation in the (β_2, γ) plane. Superdeformed prolate shapes having an axis ratio of 2:1:1 correspond to the coordinates ($\beta_2 \sim 0.6, \gamma = 0$).

2.2 Nuclear Rotations

Collective nuclear rotations about any symmetry axis are quantum mechanically forbidden, that is, the collective angular momentum $\mathbf{R}$ cannot have a component on the symmetry axis since states which undergo rotation about this axis are indistinguishable from one another and thus have no significance physically. Deformed nuclei can however rotate about any axis that is not a symmetry axis.

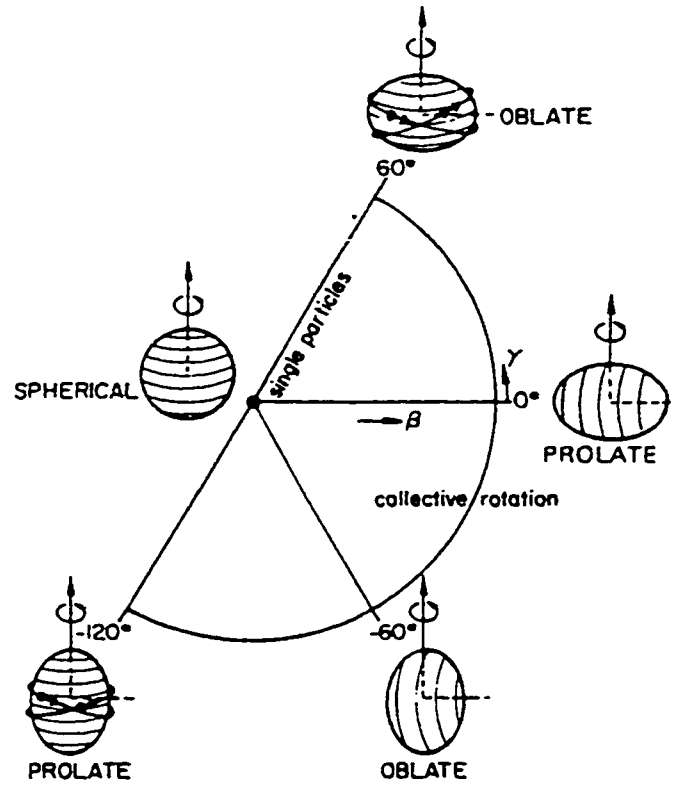

Figure 2.1: Nuclear shapes represented in the (β_2, γ) plane. Prolate and oblate shapes exhibiting collective rotations occur at $\gamma = 0$ and $\gamma = -\frac{\pi}{3}$, respectively. Collective rotations are not allowed at $\gamma = -\frac{2\pi}{3}$ and $\gamma = \frac{\pi}{3}$, however, single-particle excitations can occur. Reproduced from Ejiri and de Voigt[15].

Experimentally, rotational spectra are observed in many nuclei whose proton and neutron numbers place them in regions far from closed shells. The Hamiltonian H for such a nucleus can be separated into a sum of Hamiltonians describing its collective rotation and intrinsic motions:

$$H = H_{col} + H_{int} \tag{2.3}$$

This is known as the particle-rotor model. In terms of $\mathbf{R}$ and the moment of inertia $\mathcal{J}$, H_{col} can be written as

$$H_{col} = \frac{\hbar^2}{2\mathcal{J}_{x'}} R_{x'}^2 + \frac{\hbar^2}{2\mathcal{J}_{y'}} R_{y'}^2 + \frac{\hbar^2}{2\mathcal{J}_{z'}} R_{z'}^2 \tag{2.4}$$

The total angular momentum **I** of the nucleus (nuclei having an axis of symmetry will be considered in what is to follow) is a sum of the intrinsic angular momentum **j** and the collective angular momentum **R**,

$$\mathbf{I} = \mathbf{j} + \mathbf{R} \tag{2.5}$$

Figure 2.2 illustrates the relationship between these three quantities for a prolate shape whose symmetry axis is taken to be the z'-axis. With this choice the $R_{z'}$ component must vanish. Thus, the projection of **j** onto the z'-axis, denoted as Ω, must equal the projection of **I** onto the z'-axis, denoted as K, which follows from the assertion that no quantum-mechanical rotation is possible about a symmetry axis. Also, it must necessarily be true that $\mathcal{J}_{x'} = \mathcal{J}_{y'} \equiv \mathcal{J}$. Thus [16]

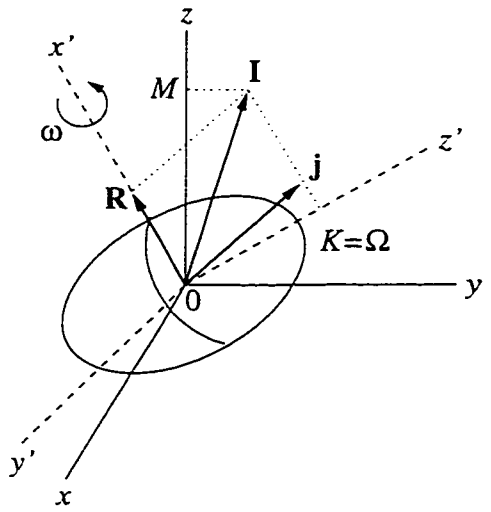

Figure 2.2: Illustration showing the relationship between the intrinsic angular momentmum **j**, the collective angular momentum **R**, and the total angular momentum **I**. Note that $\mathbf{j} = \mathbf{l} + \mathbf{s}$ where **l** and **s** are the intrinsic orbital and spin angular momenta, respectively. Note that the unprimed coordinate system is the laboratory frame and the primed coordinate system is the body-fixed frame. The z'-axis is the axis of symmetry.

$$H_{col} = \frac{\hbar^2}{2\mathcal{J}} R_{x'}^2 + \frac{\hbar^2}{2\mathcal{J}} R_{y'}^2$$

$$= \frac{\hbar^2}{2\mathcal{J}}(\mathbf{I}^2) + \frac{\hbar^2}{2\mathcal{J}}(j_{x'}^2 + j_{y'}^2 - j_{z'}^2) + H_{coup} \tag{2.6}$$

The first term in the Hamiltonian depends only on the total angular momentum and is a constant of motion. The second term acts on valence nucleons which are not part of the collective core. The third term, H_{coup}, which couples the intrinsic and rotational motions, represents the Coriolis interaction. The simple structure of rotational bands (see figure 2.3 for an illustration) tells us that terms two and three are relatively small and can be neglected in a first approximation of the symmetric rotor model. The Hamiltonian (2.6) then leads to the eigenvalues

$$E = \frac{\hbar^2}{2\mathcal{J}} I(I+1) \tag{2.7}$$

for a rotational band built on the ground state of an even-even nucleus. The I quantum number is restricted to either even or odd sequences depending on the signature (see section 2.5.1) of the states considered.

2.3 Nuclear Vibrations

Vibrations of the nucleus can be readily thought of as small oscillations of a liquid drop about an average spherical or deformed shape. The various vibrational modes are characterized by a quantum of vibrational energy called a phonon and are conveniently labeled by λ of equation (2.1). A $\lambda = 1$ vibration, known as a dipole vibration, represents a net displacement of the center of mass and such vibrations cannot result from the action of internal nuclear forces[†]. The next lowest vibrational mode, corresponding to $\lambda = 2$, is called a quadrupole vibration and is depicted in figure 2.4. The $\lambda = 2$ phonon carries 2 units of angular momentum and positive parity. Adding

[†]It should be noted that a collective excitation known as a giant-dipole resonance (GDR) exists in virtually all nuclei. GDR can be thought of as quantized oscillations of the neutron and proton densities in antiphase, the center of the two densities remaining fixed in space.

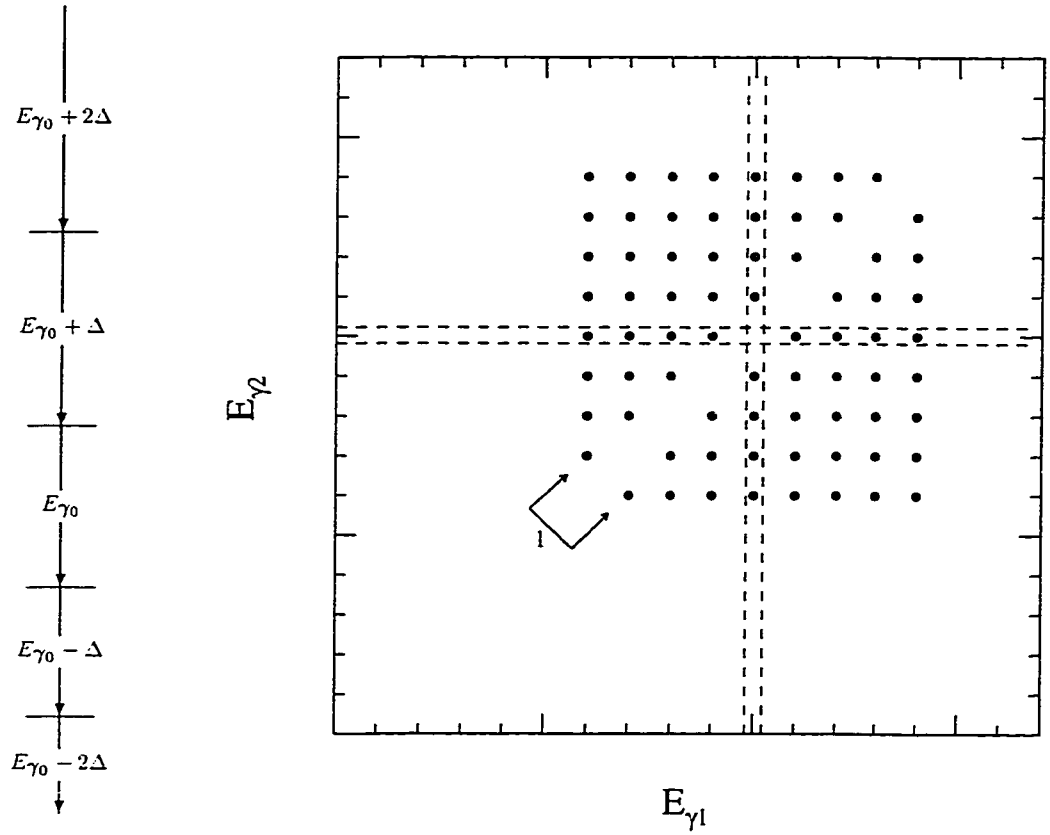

Figure 2.3: Schematic of a rotational cascade in a γ-γ correlation array (also known as a coincidence matrix). If one plots the energies of two coincident γ rays from the de-excitation of a regular rotor the points will appear on a square lattice as shown. The spacing of the lattice is fixed by the dynamic moment of inertia $\mathcal{J}^{(2)}$, see section 3.2 for a definition of $\mathcal{J}^{(2)}$. Note that the lattice is symmetric about the $E_{\gamma_1} = E_{\gamma_2}$ diagonal and that no points exist on that diagonal. Taken from [17].

a single quadrupole phonon to a 0^+ ground state of an even-even nucleus results in a 2^+ excited state and the addition of two quadrupole phonons results in a triplet of states with spins and parities of 0^+, 2^+, and 4^+ at an energy twice that of the first 2^+ excited state. The next vibrational mode is the $\lambda = 3$ octupole vibration, also depicted in figure 2.4. The $\lambda = 3$ phonon carries 3 units of angular momentum and negative parity and therefore the addition of one octupole phonon to the 0^+ ground state of an even-even nucleus results in a 3^- excited state. For nuclei in the mass

regions of interest in this Thesis, the energy of the 3^- excited state is usually somewhat higher than that of the two-quadrupole-phonon triplet. It should be pointed out at this time that combinations of both types of collective excitations can occur. For example, a rotational band can be built on a vibrational state.

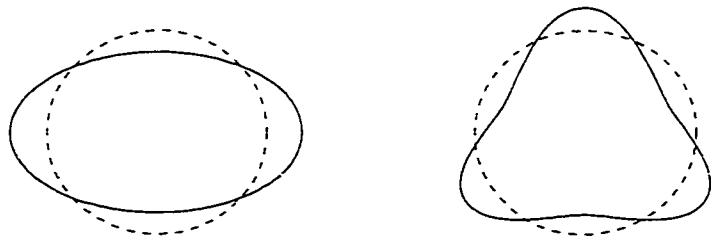

Figure 2.4: Schematic of vibrational modes of the nucleus. Shown are instantaneous views of vibrations (solid lines) about a spherical equilibrium shape (dashed lines).

2.4 The Nilsson Model

The Nilsson model [18] is a simple modification of the harmonic oscillator that provides a means of calculating single-particle orbitals in a deformed shell-model potential. In this model the single-particle Hamiltonian is taken to be

$$H_{Nilsson} = H_0 + C\mathbf{l}\cdot\mathbf{s} + D\mathbf{l}^2 \tag{2.8}$$

where the parameters C and D are empirically chosen such that the known shell-model level sequence at zero deformation is reproduced. For the case of axially symmetric deformations H_0 can be written as

$$H_0 = -\frac{\hbar^2}{2M}\nabla^2 + \frac{1}{2}M\left(\omega_\perp^2(x^2+y^2) + \omega_z^2 z^2\right) \tag{2.9}$$

where $\omega_\perp \equiv \omega_x = \omega_y$ and z is the symmetry axis. It should be pointed out that x, y, and z of equation (2.9) refer to the body-fixed axes, i.e. the primes have been

dropped for convenience. In terms of the quadrupole deformation parameter ϵ the oscillator frequencies can be written as

$$\omega_\perp = \omega_0 \left(1 + \frac{1}{3}\epsilon\right) \tag{2.10}$$

$$\omega_z = \omega_0 \left(1 - \frac{2}{3}\epsilon\right) \tag{2.11}$$

where $\hbar\omega_0 = 41A^{-1/3}$ MeV is an estimate of the oscillator frequency for spherical nuclei. The relationship between ϵ for the ellipsoid and β_2 for the quadruploid is

$$\epsilon = \frac{3}{4}\sqrt{\frac{5}{\pi}}\beta_2 - \frac{75}{224\pi}\beta_2^2 - \frac{81}{128\pi}\sqrt{\frac{5}{\pi}}\beta_2^3 + \ldots \tag{2.12}$$

In the limit of large deformation the $\mathbf{l}\cdot\mathbf{s}$ and $\mathbf{l}^2$ terms of equation (2.8) can be neglected and the wave functions are characterized by Nilsson quantum numbers, $\Omega^\pi[Nn_z\Lambda]$[†]. Here π is the parity of the single-particle orbit, $N = n_x + n_y + n_z$ is the total number of oscillator quanta, n_z is the number of quanta along the z-axis, and

$$\begin{aligned} l_z \left|\Omega^\pi[Nn_z\Lambda]\right\rangle &= \Lambda\hbar \left|\Omega^\pi[Nn_z\Lambda]\right\rangle \\ s_z \left|\Omega^\pi[Nn_z\Lambda]\right\rangle &= \Sigma\hbar \left|\Omega^\pi[Nn_z\Lambda]\right\rangle \\ \Omega &= \Lambda + \Sigma \end{aligned} \tag{2.13}$$

The energy spectrum is obtained by diagonalizing the Hamiltonian (2.8). A plot of Nilsson single-particle energies as a function of deformation is given in figure 2.5. Each single-particle level is labeled by its asymptotic quantum number $\Omega^\pi[Nn_z\Lambda]$.

2.5 The Cranking Model

The cranking model, first introduced by Inglis [20], provides a way of calculating the moment of inertia by rotating a given intrinsic wave function and evaluating the

[†]The Nilsson quantum numbers are sometimes written in the form $[Nn_z\Lambda]\Omega^\pi$.

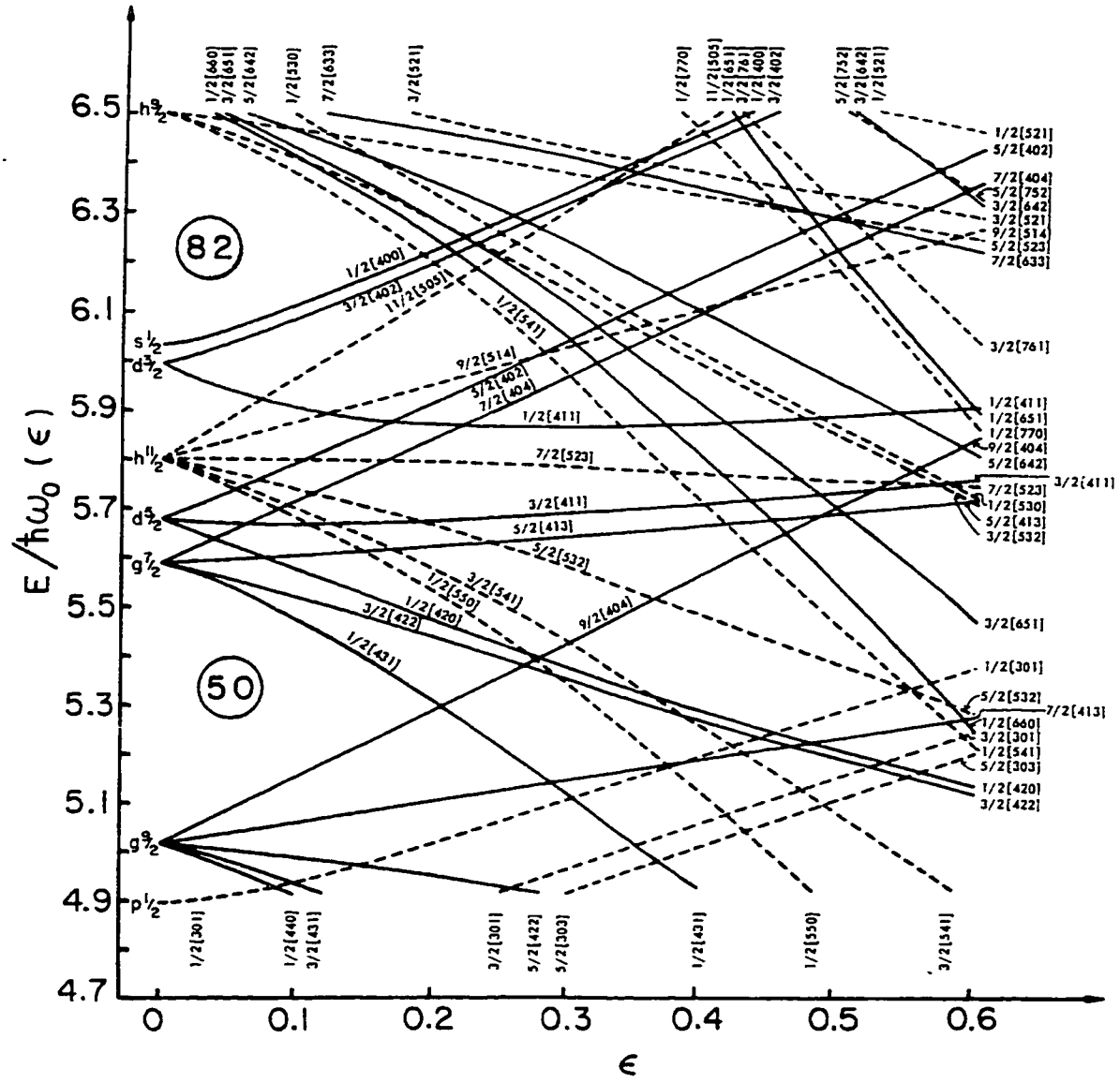

Figure 2.5: Nilsson diagram for the proton number $Z \sim 50 - 82$. Solid (dashed) lines represent positive (negative) parity orbitals. Taken from [19].

corresponding increase in energy. Given the intrinsic wave function $\phi(r,t)$, which is stationary in a rotating frame and is written in space-fixed coordinates, the time-dependent Schrödinger equation can be expressed as

$$H_{sp}\phi(r,t) = i\hbar\frac{\partial}{\partial t}\phi(r,t) \tag{2.14}$$

The wave function $\phi(r,t)$ can be related to the wave function $\phi'(r,t)$, which is stationary in the stationary frame, using

$$\phi'(r,t) = e^{i\omega t j_x}\phi(r,t) \tag{2.15}$$

where ω is the angular velocity of the rotating frame. Substituting (2.15) into (2.14) yields

$$i\hbar\frac{\partial}{\partial t}\phi'(r,t) = \left[H_{sp} - \hbar\omega j_x\right]\phi'(r,t) \tag{2.16}$$

where the operator in the square brackets and its eigenvalues are known as the single-particle Routhians. By summing over all occupied single-particle states we get the stationary-state wave equation

$$\left[H - \hbar\omega J_x\right]\phi'(r) = E(\omega)\phi'(r) \tag{2.17}$$

where $\mathcal{R} = H - \hbar\omega J_x$ is known as the total Routhian operator, $J_x = \sum_{k=1}^{A}(j_x)_k$, and

$$\phi'(r,t) = e^{-iE(\omega)t/\hbar}\phi'(r) \tag{2.18}$$

The moment of inertia for a given state $|0\rangle$ is then [20]

$$\mathcal{J} = 2\hbar^2 \sum_{i\neq 0} \frac{|\langle i|J_x|0\rangle|^2}{E_i - E_0} \tag{2.19}$$

where i labels the many-particle states of the A nucleons in the deformed potential and E_i are the excitation energies.

2.5.1 The Parity and Signature Quantum Numbers

The Routhian operator $\mathcal{R} = H - \hbar\omega J_x$ is invariant with respect to:

- An inversion of the axes $\mathbf{r} \rightarrow -\mathbf{r}$.
- A rotation about the x axis by an angle of 180°.

The invariance of $\mathcal{R}$ for these two symmetries and the fact that it is not invariant

under time reversal implies that only two quantum numbers are conserved as the nucleus rotates. The first is the parity ($\pi = \pm 1$) and the second is the signature. The signature, α, is defined by

$$\exp\left(\frac{-i\pi j_x}{\hbar}\right)|\psi'\rangle = \exp\left(-i\pi\alpha\right)|\psi'\rangle \tag{2.20}$$

where $\pi = 180°$. States having a total angular momentum differing by $2\hbar$ have the same signature. For even nuclei:

$$\begin{aligned} \alpha = 0 \quad &: \quad I = 0, 2, 4, \ldots \\ \alpha = 1 \quad &: \quad I = 1, 3, 5, \ldots \end{aligned} \tag{2.21}$$

and for odd nuclei:

$$\begin{aligned} \alpha = 1/2 \quad &: \quad I = 1/2, 5/2, 9/2, \ldots \\ \alpha = -1/2 \quad &: \quad I = 3/2, 7/2, 11/2, \ldots \end{aligned} \tag{2.22}$$

2.6 Total Routhian Surface

It is possible to calculate the total potential energy for a nucleus as a function of its deformation parameters (i.e. β_2, β_4, and γ)[†] for a given particle configuration. The resulting surface plot is known as a Total Routhian Surface (TRS) [21] and is calculated for given values of rotational frequency ω. By studying TRS diagrams one can determine the deformation parameters and rotational frequency at which the overall potential energy is a minimum. This provides a means by which the shape of nuclei can be predicted and can therefore serve as a starting point in the search for superdeformation.

[†]The β_4 parameter is known as a hexadecapole deformation parameter and corresponds to $\lambda = 4$ in equation (2.1), just as β_2 corresponds to $\lambda = 2$ in that equation.

Chapter 3

Experimental Techniques

"Now, we have such a marvelous loss of boundaries that your criticism of a happening could be a piece of music, or a scientific experiment, or a trip to Japan, or a trip to your local shopping market."

John Cage (1912-1992) [22]

The previous chapter dealt with theoretical concepts of high-spin physics that are helpful in the interpretation of experimental data. This chapter concerns the experimental techniques of high-spin nuclear physics. It begins with an introduction to fusion-evaporation reactions and population of high-spin states. Next, experimental observables which can be extracted from data, and are therefore of great importance in the analysis process, are outlined. Lastly, the various high-spin gamma-ray spectrometers that were used in the experiments which will be described later in this Thesis are briefly introduced.

3.1 Fusion-Evaporation Reactions

In the first stage of a fusion-evaporation reaction heavy ions ${}^{A_1}_{Z_1}\mathrm{X}$ are accelerated towards a target of nuclei ${}^{A_2}_{Z_2}\mathrm{Y}$. The two nuclei will fuse to form the compound nu-

cleus [23] ${}^{A_1+A_2}_{Z_1+Z_2}V^*$ having an excitation energy E^* and maximum classical angular momentum l_{max} if the following two conditions are met. The energy of the beam of heavy ions must be sufficiently high to overcome the Coulomb barrier of the reaction (tunneling through the barrier is of course possible as will be seen in chapter 4) and, at the same time, the impact parameter b of the system must be sufficiently small, otherwise the two nuclei will collide inelastically. For very large values of b elastic scattering will occur.

The value of l_{max} may be estimated as [24]

$$l_{max} = 0.219 R_{int} \left[\mu(E_{c.m.} - V(R_{int}))\right]^{1/2} \tag{3.1}$$

where μ is the reduced mass in atomic mass units and $E_{c.m.}$ and $V(R_{int})$ are in units of MeV. R_{int}, the approach distance in fm, may be estimated as

$$R_{int} = 1.16\left(A_1^{1/3} + A_2^{1/3} + 2\right) \tag{3.2}$$

and the Coulomb barrier $V(R_{int})$ is taken to be

$$V(R_{int}) = 1.44\frac{Z_1 Z_2}{R_{int}} \tag{3.3}$$

The center of mass energy $E_{c.m.}$ is related to the excitation energy E^* and the Q-value[†] of the reaction by

$$E_{c.m.} = E^* - Q \tag{3.4}$$

and it is related to the beam energy E_{lab} by

$$E_{c.m.} = \frac{A_2}{A_1 + A_2} E_{lab} \tag{3.5}$$

Compound nucleus formation takes about 10^{-22} seconds and is depicted in the upper portion of figure 3.1.

[†]The Q-value is the difference in binding energy of the reactants and the compound nucleus.

The compound nucleus will now either fission or begin to evaporate particles, this is the second stage of the fusion-evaporation process. The fission process depends on the height of the fission barrier which itself depends on the angular momentum, A, and Z of the compound nucleus. Particle evaporation, i.e. emission of neutrons, protons, and alpha particles, provides the quickest means of cooling the compound nucleus. Fusion-evaporation reactions are usually represented either by the expression

$$ {}^{A_1}_{Z_1}\mathrm{X} + {}^{A_2}_{Z_2}\mathrm{Y} \rightarrow {}^{A_1+A_2}_{Z_1+Z_2}\mathrm{V}^* \rightarrow {}^{A_3}_{Z_3}\mathrm{W} + x \tag{3.6} $$

or, in the more compact format,

$$ {}^{A_2}_{Z_2}\mathrm{Y}({}^{A_1}_{Z_1}\mathrm{X}, x){}^{A_3}_{Z_3}\mathrm{W} \tag{3.7} $$

where x denotes the evaporated particles. The residue corresponding to the emission of x equal to three neutrons, for example, is known as the 3n exit channel. For the compound nuclei of interest in this Thesis neutron evaporation occurs more readily because protons and alphas must first overcome a relatively large Coulomb barrier. It takes place between the approximate times of 10^{-20} and 10^{-19} seconds depending on E^* of the compound system. Fission and neutron evaporation will have approximately the same probability of occurrence when the fission barrier is equal to the neutron binding energy which is about 8 MeV.

As particles are emitted the excitation energy of the compound nucleus is reduced by the binding and kinetic energies of the particles and small amounts of angular momentum are carried away. The kinetic energy and angular momentum carried off by evaporated particles may be calculated by statistical models, however, for neutron evaporation a fairly good estimate is 1.5 MeV of kinetic energy and $1\hbar$ of angular momentum per neutron. Particle evaporation can continue as long as there are available states in the residual nuclei. The yrast state is defined as the minimum

energy state for a given value of angular momentum. The yrast line connects the yrast states in a E^* versus l plot and no states exist below this line. Residues populated at higher spins must necessarily emit fewer particles and as a result several reaction channels having different angular-momentum distributions will be present, as shown in figure 3.1.

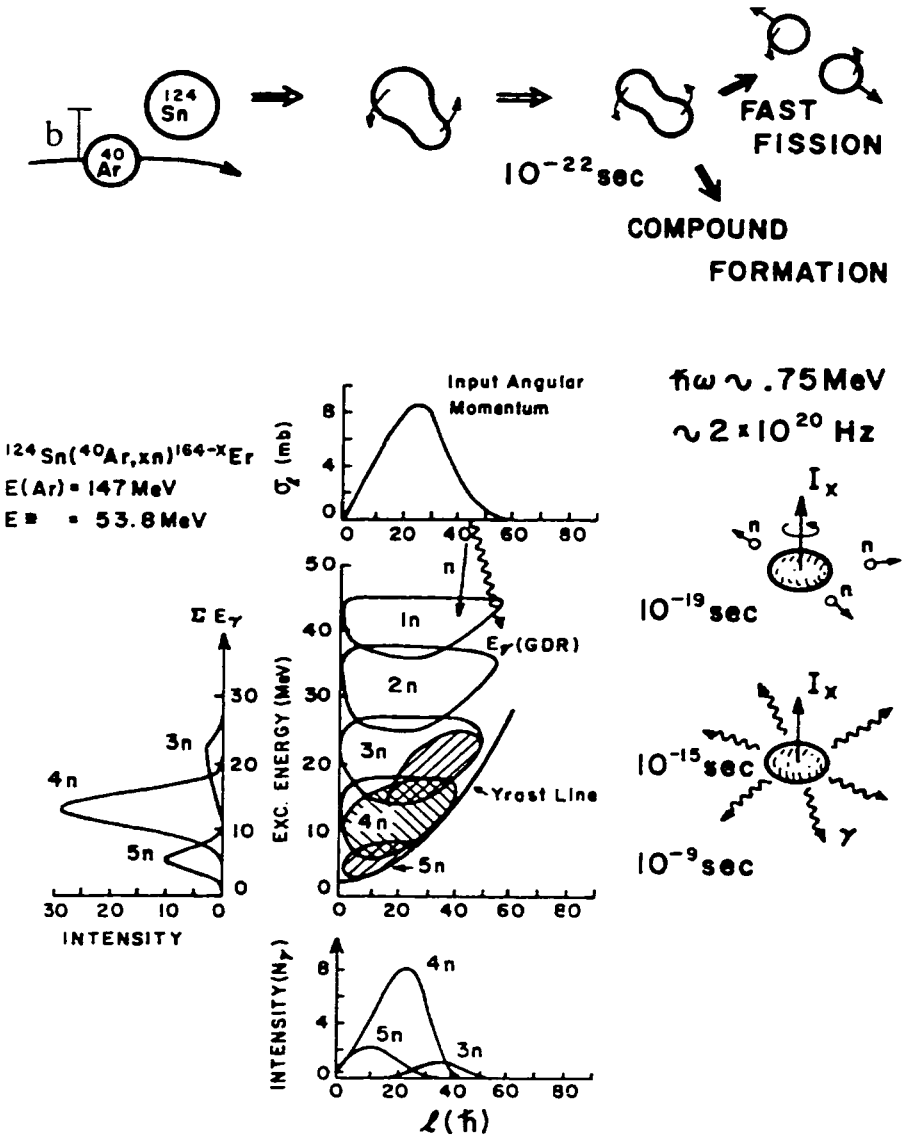

Figure 3.1: Statistical-model calculations for a heavy-ion fusion-evaporation reaction leading to high-spin states. Taken from [25].

3.1.1 Population of High-Spin States

The third stage of the fusion-evaporation reaction is γ-ray emission from the residual nucleus. Gamma-ray cooling begins with the emission of statistical γ rays whose emission probabilities are strictly determined by the nuclear level density. These γ rays are generally $E1$ in character and as such remove little angular momentum. Cooling of the nucleus continues in this manner until the quasi-continuum (sometimes referred to as the continuum) region is reached. In the continuum predominantly stretched $E2$ transitions occur; these are transitions in which the change in angular momentum is equal to the multipolarity of the transition. Although quantum states are intrinsically resolvable in this region the vast number of paths by which γ rays can decay makes it impossible to measure individual states. It is not until the nucleus is close to the yrast line that individual γ rays can be resolved.

3.2 Experimental Observables

When analyzing experimental data it is often useful to make analogies to classical rotating systems. The rotational frequency ω is a useful quantity to extract from a rotational band, however, since it cannot be measured directly it must be inferred from the classical relation

$$\omega = dE/dI \tag{3.8}$$

where E is the rotational energy and I is the angular momentum of a rotating body. When equation (3.8) is quantized the following expression is found:

$$\hbar\omega = \frac{E(I) - E(I-2)}{I_x(I) - I_x(I-2)} \tag{3.9}$$

where

$$I_x = \sqrt{I(I+1) - K^2} \tag{3.10}$$

is the projection of the total angular momentum on the rotation axis.

In a similar fashion to the above, moments of inertia (denoted by $\mathcal{J}$s) can be inferred from classical analogues. The kinematic moment of inertia is expressed as

$$\mathcal{J}^{(1)} = \frac{\hbar^2}{2}\left(\frac{\partial E}{\partial(I_x^2)}\right)^{-1} = \hbar\frac{I_x}{\omega} \tag{3.11}$$

and can be estimated from the difference $E_\gamma = E(I) - E(I-2)$ for a stretched $E2$ γ-ray transition between the states of angular momenta I and $I-2$. It can be shown that a good approximation is

$$\mathcal{J}^{(1)} = \frac{\hbar^2}{2E_\gamma}(4I-2) \tag{3.12}$$

The dynamic moment of inertia is expressed as

$$\mathcal{J}^{(2)} = \hbar^2\left(\frac{\partial^2 E}{\partial {I_x}^2}\right)^{-1} = \hbar\frac{\partial I_x}{\partial\omega} \tag{3.13}$$

and can be evaluated from a two γ-ray cascade $(I+2) \rightarrow I \rightarrow (I-2)$ with the expression

$$\mathcal{J}^{(2)} = \frac{4\hbar^2}{\Delta E_\gamma} \tag{3.14}$$

where $\Delta E_\gamma = E_{\gamma_1} - E_{\gamma_2}$. The independence of $\mathcal{J}^{(2)}$ on the spins of the states makes it a desirable quantity to extract from experiments dealing with superdeformation since in most cases one cannot experimentally determine the spins of superdeformed states unambiguously.

3.3 High-Spin Gamma-Ray Spectrometers

The experiments described in this Thesis were performed at three different institutes with three different γ-ray spectrometers. Given below are brief descriptions of the arrays used with emphasis made on the differences between the spectrometers. Detailed descriptions of detector operations can be found in the references cited in the following sections and in references [17, 26, 27].

3.3.1 The 8π Spectrometer

The 8π Spectrometer [28, 29], shown in figure 3.2, was located at AECL Chalk River Laboratories at the time of the experiment presented in chapter 6. It comprises 20 hyperpure germanium (HPGe) detectors designed to measure the energies of two coincident γ rays from a fusion-evaporation reaction. Germanium detectors are renown for their ability to detect γ ray energies with high resolution, but they have a low detection efficiency. Most of the interactions of a γ ray hitting a detector occur via the Compton effect. Thus, γ rays often scatter out of HPGe detector crystals and deposit only some of their energy in the crystals. Such events are of little interest in experiments and are therefore rejected using anti-Compton shields. Compton suppression is done with highly efficient bismuth germanate ($Bi_4Ge_3O_{12}$ or simply BGO) detectors that surround the HPGe detectors. Only events for which a given HPGe detector fires in anti-coincidence with the BGO shield are collected.

The 8π Spectrometer also comprises a 71-element BGO ball that is used as a γ-ray calorimeter and multiplicity detector. Since the HPGe detectors have high energy resolution but low efficiency it is complimentary to have an inner ball that has a high efficiency. The HPGe detectors make up about 5% of the total solid angle with the BGO ball covering the remaining 95%. The target is viewed by the HPGe detectors through perforations in the BGO ball and detected γ rays are doppler shift corrected according to the relation[†]

$$\begin{aligned} E'_\gamma &= \frac{\left(1+\beta_{||}cos(\theta)\right)E_\gamma}{\sqrt{1-\beta^2}} \\ &\approx \left(1+\beta_{||}cos(\theta)\right)E_\gamma \end{aligned} \tag{3.15}$$

Here E'_γ is the γ-ray energy in the laboratory frame, E_γ is the γ-ray energy in the

[†]Gamma rays that are detected with the GammaSphere and GASP spectrometers are also doppler shift corrected according to this relation.

frame of the recoiling nucleus, and θ is the detector angle with respect to the beam axis. The velocity of the recoiling compound nucleus is $v = \beta c$ (where c is the speed of light in vacuum) and $\beta_{||}$ is the component of β along the beam axis.

Energy and efficiency calibrations of the HPGe detectors are performed with the standard radioactive sources ^{152}Eu and ^{133}Ba. The absolute photopeak detection efficiency [27] for the HPGe detectors of the 8π Spectrometer is $\sim$ 0.8% [30] for 1 MeV γ rays. Beams used to bombard targets placed at the center of the array were provided by the Tandem Accelerator Superconducting Cyclotron (TASCC) facility.

3.3.2 The GammaSphere Multi-Detector Array

At the time of the experiment presented in chapter 7 the GammaSphere [31] multi-detector array was located at the Ernest O. Lawrence Berkeley National Laboratory. GammaSphere was designed to have high efficiency detection for high-fold events, i.e. events for which three of more γ rays have been detected. This is done by maximizing the solid angle viewed by the detectors that make up GammaSphere. GammaSphere has an absolute photopeak efficiency of $\sim$ 10% for 1.33 MeV γ rays. The array has no inner ball like that of the 8π Spectrometer but when completed will consist of 110 large-volume Compton-suppressed HPGe detectors (at the time of the experiment presented in chapter 7, 97 of the possible 110 detectors were in place). Energy and efficiency calibrations of the detectors are performed with standard radioactive sources. Beams were provided by the 88-Inch Cyclotron.

3.3.3 The GASP Spectrometer

The GASP [32](Grande Array per SPecttroscopia) spectrometer is located at the Legnaro National Laboratory. It is similar to GammaSphere in that high efficiencies can be obtained for high-fold events and it resembles the 8π Spectrometer since it too

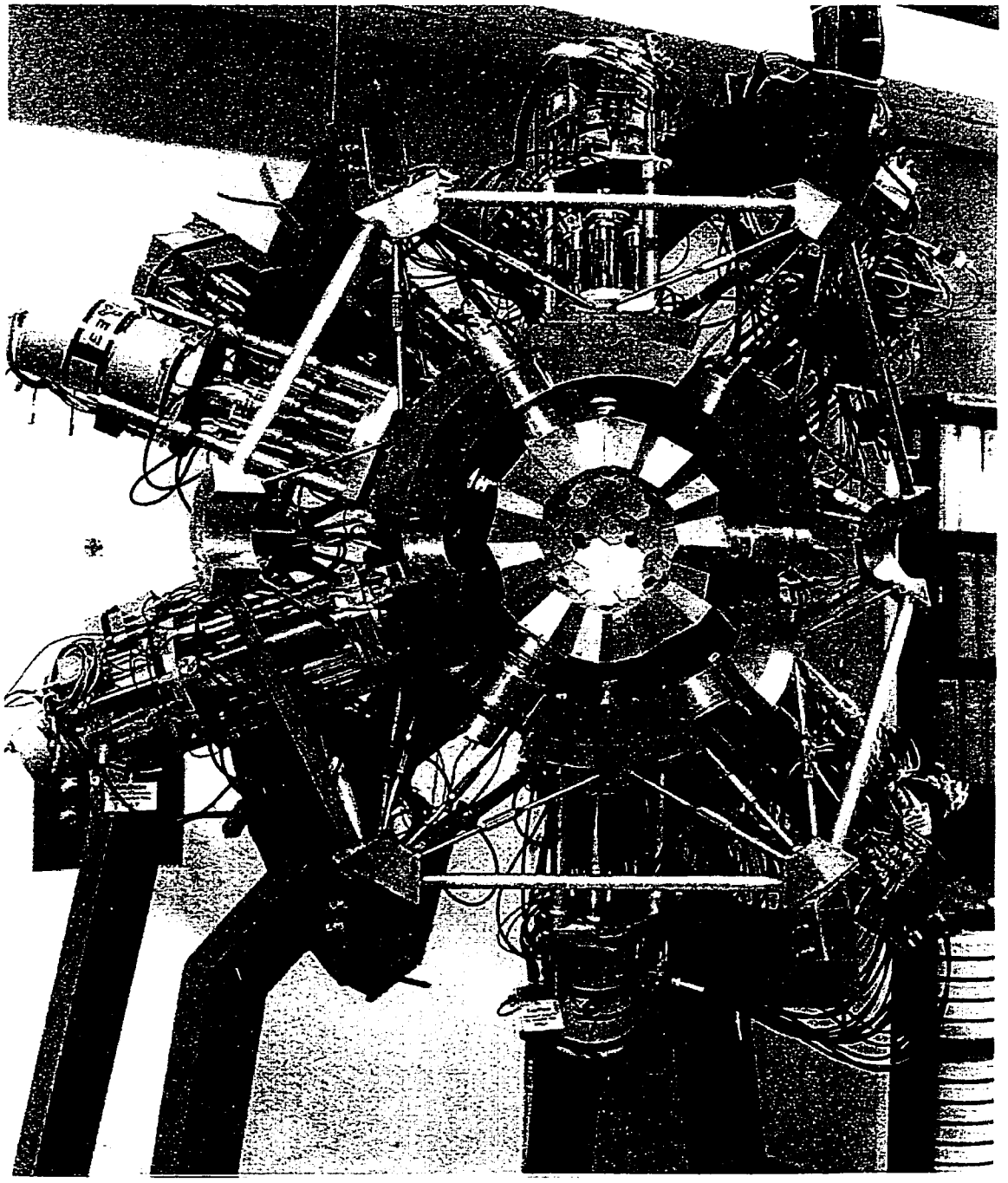

Figure 3.2: Photograph of half of the 8π Spectrometer. Visible are a number of the Compton-suppressed HPGe detector view ports (seen as the small black holes) and half of the BGO ball.

has an inner ball of BGO crystals. More specifically, GASP consists of an array of 40 large-volume Compton-suppressed HPGe detectors and an inner ball of 80 BGO crystals which cover about 10% and 80% of the total solid angle, respectively. The absolute photopeak efficiency for the HPGe detectors of the GASP spectrometer is $\sim$ 3% for 1.33 MeV γ rays. The charged-particle detector ISIS [33], developed by a Padova-Legnaro collaboration, was also implemented in the experiment discussed in chapter 5. It consists of 40 ΔE-E silicon telescopes (130 μm and 1000 μm thick respectively) covering a geometrical solid angle $\sim$ 90% of 4π. Beams used to bombard targets placed at the center of the array are provided by the Tandem-Alpi accelerator.

Chapter 4

Computer Modelling of Fusion-Evaporation Reactions

"Logic is the art of going wrong with confidence."

Joseph Wood Krutch (1893-1970) [34]

In this chapter the modelling of fusion-evaporation reactions via the use of computer simulations will be described. Each section is designed to provide the reader with an introduction to the codes employed in this Thesis as well as supply a complete reference list for any further reading that may be of interest. The chapter opens with a discussion of dissipative collision calculations. Next, coupled-channel calculations and the study of barrier penetration in the fusion of heavy ions are examined. Lastly, statistical-model particle-evaporation calculations will be touched upon briefly.

4.1 Dissipative Collision Calculations and the Code HICOL

Dissipation is the irreversible transformation of accessible energy into another form. The conversion of kinetic and potential energies of a nuclear reaction into intrinsic energy (i.e. single-particle excitations) is partly irreversible and is an example of

dissipation. Heavy nuclei are quantal systems that have too many particles to be considered few-body systems, yet too few particles to be considered statistical systems. As such, concepts like friction and diffusion were never incorporated into the theory of atomic nuclei. However, experimental measurements, although largely incomplete, have shown evidence for dissipative behaviors in observables such as excitation energies of target/projectile nuclei in inelastic scattering experiments and new theories were needed.

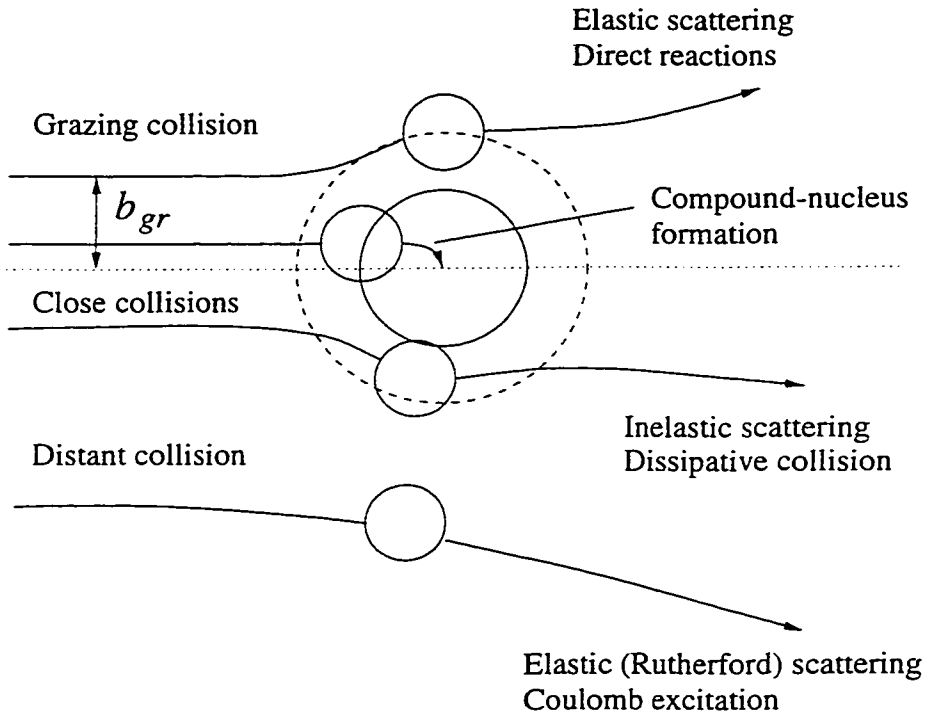

Figure 4.1: Schematic of various types of collisions. Each collision is associated with a different impact parameter, b, and angular momentum $l = b(2\mu E_{c.m.})^{1/2}$. The trajectory at which nuclear interaction between the target and projectile becomes considerable is determined by the grazing impact parameter, b_{gr}. Dissipative collision calculations are necessary whenever close collisions (i.e. $b < b_{gr}$) are involved. Adapted from [35].

Depicted in figure 4.1 are various types of collisions, it is necessary to take dissipation into account whenever close collisions (i.e. $b < b_{gr}$) are involved. Dissi-

pative effects are known to delay fusion and fission processes of heavy-ion reactions. Calculations based on dissipative dynamics [36, 37] provide a means of determining the fusion time of a given reaction. The fusion time may be defined as the time required for the thermal energy of the system to reach some specified fraction of its final value (see for example [38]), where time zero is taken to be the time at which the nuclei of interest first make contact. It has been found [36] that fusion times are strong functions of the mass asymmetry of the entrance channel as long as the fissility of the system is large, where the fissility is taken to be proportional to Z^2/A of the compound nucleus.

The theory behind dissipative collision calculations is far beyond the scope of this Thesis. However, detailed derivations of the equations of motion needed to describe the collisions can be found in reference [37]. In this Thesis dissipative collision calculations were performed with the computer code HICOL [39] which is based on the wall-plus-window dissipation formalism [36, 37].

4.2 Coupled-Channel Calculations and the Code CCFUS

The study of barrier penetration gained interest in low energy heavy-ion fusion reactions when it was noted that cross sections were drastically underpredicted by standard potential barrier penetration calculations, see for example reference [40] and references therein. Since the fusion of heavy nuclei is too complex to be described by the collision of rigid spheres, a model that has been successful in lighter mass systems, it is necessary to consider how the nuclei vibrate and/or exchange particles as they approach one another in the fusion process. Figure 4.2 depicts a collision in which the target nucleus is considered to be a good vibrator. As the projectile

approaches the target, excitations may occur which result in changes in the Coulomb barrier of the reaction. The lowering of the Coulomb barrier obviously results in easier compound-nucleus formation.

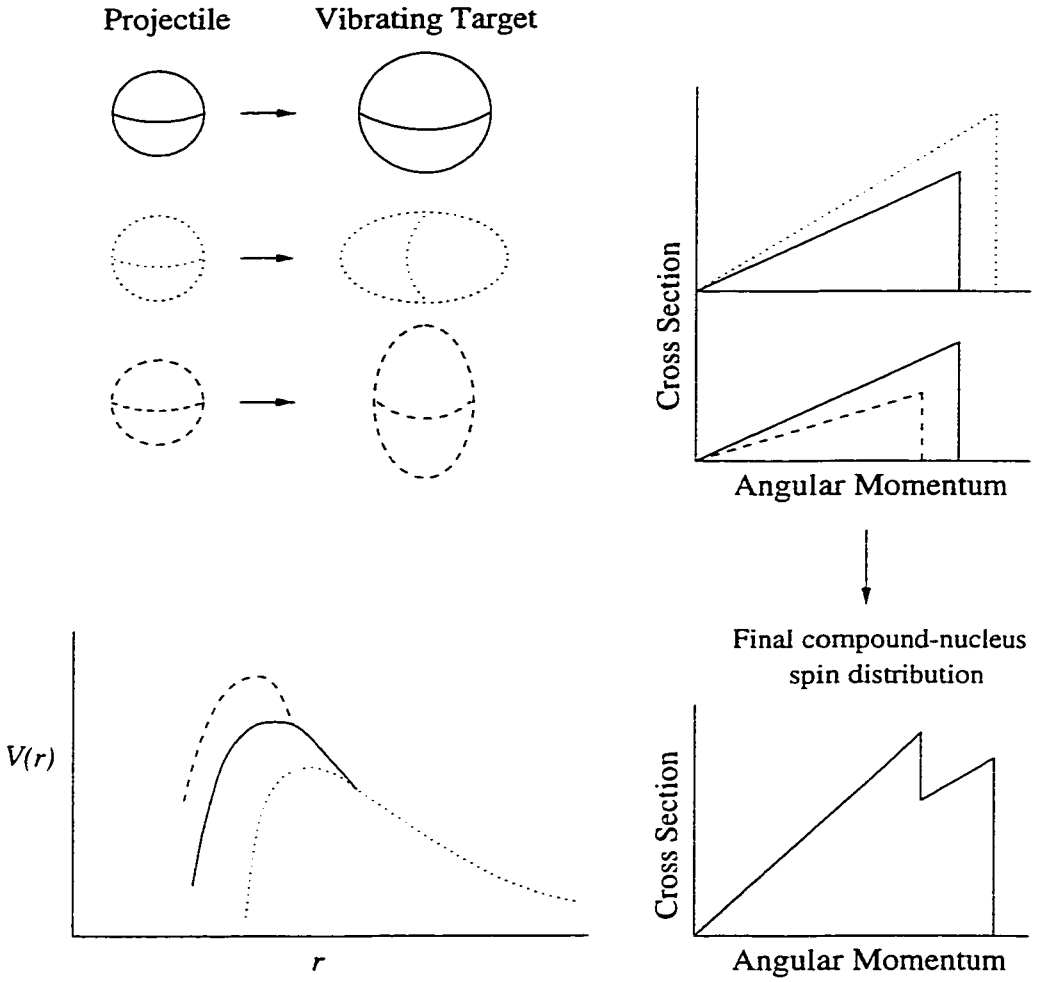

Figure 4.2: Schematic of a heavy-ion collision involving a target nucleus that is considered to be a good vibrator. The bottom left of the figure, adapted from [41], shows how the Coulomb barrier of the reaction changes as a function of the orientation of the two nuclei. The right-hand side of the figure depicts the resulting compound-nucleus spin (angular-momentum) distribution.

Coupling to inelastic excitation channels (i.e. vibrations) can significantly modify the angular-momentum distributions of compound nuclei and since these distributions are essential for describing the decay of a given compound nucleus, it

is vital to determine them accurately. The computer code CCFUS [42] solves this problem by treating the various inelastic excitation and transfer reaction channels as independent modes which couple to the initial ground states of the nuclei involved in a reaction. Diagonalization of the interaction, at the Coulomb barrier, uncouples the wave equations corresponding to these modes and by summing over the transmission probabilities for the eigenbarriers a total transmission probability can be obtained. An illustration of how channel coupling affects the transmission is shown in figure 4.3. Detailed explanations of the theory involved in calculating transmission coefficients and compound-nucleus angular-momentum distributions are given in references [43, 44, 45, 46].

Coupling strengths, F, for inelastic excitations to vibrational states are calculated following the formula [42]:

$$F = \frac{\beta_\lambda}{\sqrt{4\pi}} \left[-R \frac{\partial U}{\partial r}(r_B) + \frac{3 Z_1 Z_2 e^2}{(2\lambda+1)} \frac{R^\lambda}{r_B^{\lambda+1}} \right] \tag{4.1}$$

Here β_λ is the deformation parameter, λ is the multipolarity of the transition, R is the radius of the excited nucleus, and Z_1 and Z_2 are the atomic numbers of the two nuclei. The empirical nuclear potential, U, is taken from reference [47] and the position of the Coulomb barrier, r_B, is determined by [47]

$$U(r_B) = -\frac{\alpha}{r_B} \frac{Z_1 Z_2 e^2}{r_B} \tag{4.2}$$

In other words, U is used with an adjustable strength α to define the Coulomb barrier. Given in table 4.1 are energies and deformation parameters for the first 2^+ and 3^- excited vibrational states (see references [48] and [49], respectively, for example) of nuclei of interest in this Thesis.

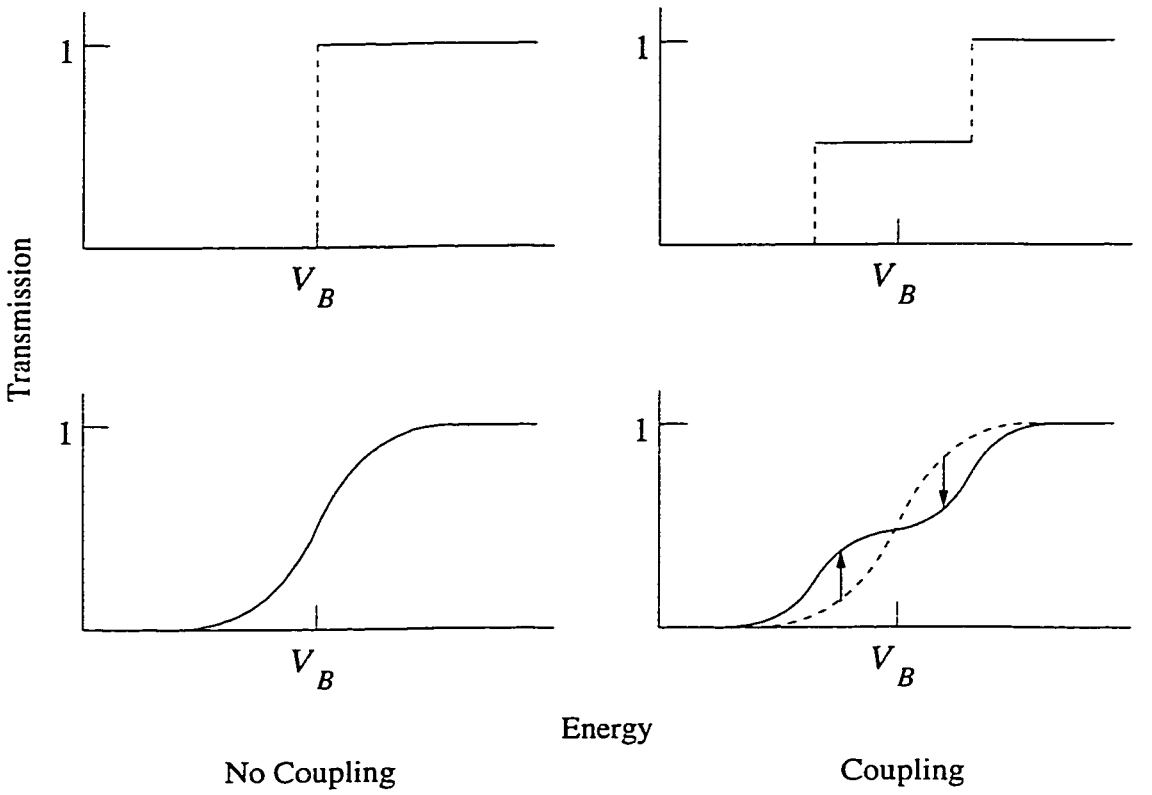

Figure 4.3: Schematic of how channel coupling (e.g. a two-channel problem) affects the transmission probability. Note that the transmission increases at energies below the barrier and decreases at energies above the barrier. The upper portion of the figure represents the classical limits while the lower portion shows the smoothing effects of quantum mechanics. Adapted from [43].

4.3 Statistical-Model Particle-Evaporation Calculations and the Code evapOR

Throughout this Thesis the results of the various heavy-ion fusion experiments are compared to predictions made with the Monte Carlo evaporation code evapOR [50] which is an extended version of the code PACE2 (Projection Angular-momentum Coupled Evaporation) [51]. Presented below is an outline of how particle-evaporation calculations are performed. Details of this can be found in references [51, 52].

The partial cross section for compound-nucleus formation at angular momen-

Table 4.1: Energies and deformation parameters for the first 2^+ and 3^- excited vibrational states of nuclei of interest in this Thesis.

Nucleus	β_2 : Energy (MeV)	β_3 : Energy (MeV)
^{26}Mg	0.48 : 1.81	0.18 : 6.88
^{28}Si	0.40 : 1.78	0.24 : 6.88
^{64}Ni	0.22 : 1.34	0.23 : 3.56
^{74}Ge	0.29 : 0.60	0.16 : 2.54
^{76}Ge	0.27 : 0.56	0.15 : 2.69
^{112}Cd	0.18 : 0.62	0.17 : 2.01
^{124}Sn	0.11 : 1.13	0.12 : 2.61

tum l may be determined by

$$\sigma_l = \frac{\lambda^2}{4\pi}(2l+1)T_l \tag{4.3}$$

where λ is the reduced wavelength. The transmission coefficients T_l may be approximated by

$$T_l = \frac{1}{1+\exp\left(\frac{l-l_{max}}{d}\right)} \tag{4.4}$$

where l_{max} [53] is chosen such that the measured total fusion cross section

$$\sigma_{fus} = \sum_{l=0}^{\infty} \sigma_l \tag{4.5}$$

is reproduced. The diffuseness, d, is obtained from optical-model calculations. The total fusion cross section σ_{fus} is similar to the sharp cut-off approximation but with some diffuseness at high angular momenta. The input fusion cross section for evapOR may also be taken from the output of CCFUS calculations. In cases where coupled-channel effects are important this is of course preferable.

The decay rate, $R_x dE_x$, for emitting a particle x from an excited nucleus i with excitation energy E_i, angular momentum I_i, and parity π_i, to form a product

nucleus f (at E_f, I_f, π_f) is [52]

$$R_x(E_i, I_i; E_f, I_f, s_x)dE_x = \frac{\rho_f(E_f, I_f, \pi_f)}{2\pi\hbar\rho_i(E_i, I_i, \pi_i)} \sum_{S=|I_f - s_x|}^{I_f+s_x} \sum_{l=|I_i-S|}^{I_f+S} T_l^x(E_x)dE_x \tag{4.6}$$

Here E_x is the kinetic energy of particle x having a spin of s_x and an orbital angular momentum of l. The channel spin is given as

$$S = I_f \oplus s_x \tag{4.7}$$

and conservation of energy states that

$$E_i = E_f + E_x + \text{separation energy of } x \tag{4.8}$$

The transmission coefficients T_l^x for the scattering of particle x on nucleus f are obtained from the optical model and may be used in equation 4.6, to calculate particle emission probabilities, by virtue of the reciprocity theorem [54].

For a γ decay [52]

$$R_\gamma(E_i, I_i; E_f, I_f)dE_\gamma = \frac{\rho_f(E_f, I_f, \pi_f)}{2\pi\hbar\rho_i(E_i, I_i, \pi_i)} \sum_l E_\gamma^{2l+1} F_l(E_\gamma)dE_\gamma \tag{4.9}$$

where l is now the multipolarity of the γ ray and $E_\gamma^{2l+1}F_l(E_\gamma)$ are energy dependent transition strengths.

The level density used in the above expressions, given as a function of energy E and spin I, is

$$\rho(E, I) = \rho_0(U)(2I+1)\exp\left(2\sqrt{a\,(U - E_{rot}(I))}\right) \tag{4.10}$$

where $U = E - P$. P is the pairing energy and a (known as the "little-a" parameter) is a parameter which determines the energy dependence of the level density. The level density at zero spin is denoted as $\rho_0(U)$ and $E_{rot}(I)$ determines the yrast line; in this Thesis these two parameters are taken from the Gilbert and Cameron formalism [55].

The decay rate for fission R_{fis} does not depend on the level densities (or other statistical properties) of the residual nuclei, in contrast to R_x and R_γ. Instead it depends on properties of the nucleus at the point where fission occurs; this point is known as the saddle point. The transmission coefficients are taken to be equal to one if the total available energy is greater than the fission barrier (or the saddle-point energy), otherwise they are set to zero. Thus, for fission [56]

$$R_{fis}(E_i, I_i; E_f, I_f) = \frac{\rho(E_f, I_f)}{2\pi\hbar\rho(E_i, I_i)} \tag{4.11}$$

with

$$E_f = E_i - E_{fis}(I_i) - E_s \tag{4.12}$$

Here $E_{fis}(I_i)$ is the fission barrier (or the saddle-point energy) and E_s is the kinetic energy at the saddle point.

Chapter 5

Superdeformation in ^{147}Tb

"What this country needs is a good five-cent cigar."

Thomas Riley Marshall (1854-1925) [57]

Stable nuclear shapes are often related to the existence of shell gaps, with superdeformed shapes being no exception. The systematic study of the gadolinium isotopes illustrated how the phenomenon of superdeformation may be related to the presence of intruder orbitals and shell gaps [58]. The work presented in this chapter begins to establish a link between superdeformation in ^{145}Tb and superdeformation in ^{150,151}Tb. The yrast superdeformed band in ^{145}Tb is known [59] to have one proton in the $N = 6$ intruder orbital while the yrast superdeformed bands in ^{150,151}Tb are known [60, 61] to have three protons in the $N = 6$ intruder orbitals. Thus, a change in the particle configuration must take place somewhere along the chain of the terbium isotopes. Such a change does not occur in the gadolinium chain (the known yrast superdeformed bands in the gadolinium isotopes all have two protons in the $N = 6$ intruder orbitals). The systematics of particle configurations in the terbium isotopes are expanded in this chapter by studying the properties of a newly discovered superdeformed band in the nucleus ^{147}Tb. One purpose of this chapter is

to provide an introduction to superdeformation. Much of the material presented in this chapter has been published in *Physical Review C* [2].

5.1 Experimental Setup

The experiment was performed at the Legnaro National Laboratory with the GASP spectrometer in conjunction with the charged-particle detector ISIS. The reaction was $^{51}V+^{100}Mo$ at a bombarding energy of 230 MeV producing ^{147}Tb after the evaporation of four neutrons. The target consisted of two foils of $\sim$500 $\mu g/cm^2$ of ^{100}Mo. Approximately 10^9 γ-γ-γ Ge coincidence events were collected in eight days of beam time.

5.2 Data Analysis and Results

In the off-line analysis events were selected with the conditions that no charged particles were detected in ISIS and that at least three Compton-suppressed HPGe detectors and ten detectors of the inner BGO ball fired in coincidence. The computer code ANDband [62] was used to search the resulting γ-γ-γ data set for regularly spaced bands and the data analysis program LEVIT8R [63] was employed for building level schemes. Known superdeformed bands in ^{143}Eu [64], ^{147}Gd [58, 65], and possibly ^{146}Gd [58, 66] were found in the ANDband search, indicating that some channel leakage had occured even with ISIS being employed, as well as a new superdeformed band consisting of 9 transitions with an average spacing of $\sim$ 57 keV. The new band was also observed in an analysis of two-fold coincidence events. This band was assigned to a neutron exit channel (often refered to as an xn channel) because its strength was greater than any of the known bands of the charged particle channels. Furthermore, the new band was tentatively assigned to either the 4n or 5n exit channel, correspond-

ing to ^{147}Tb or ^{146}Tb, respectively, since the entry conditions for other xn channels were not suitable for significantly populating superdeformed bands [58, 67]. No other new superdeformed bands were found.

No high-spin transitions have yet been identified in ^{146}Tb and it was therefore useful to perform a second set of experiments to assign the new band to either ^{146}Tb or ^{147}Tb. The two nuclei were studied with the reactions ^{113}Cd(^{37}Cl, 4n)^{146}Tb and ^{114}Cd(^{37}Cl, 4n)^{147}Tb at bombarding energies of 179 and 176 MeV, respectively. The ^{113}Cd and ^{114}Cd targets each consisted of a stack of two foils $\sim$600 μg/cm^2 thick, and γ rays were detected with the 8π Spectrometer. The 8π Spectrometer data sets provided information regarding the K distributions (where K is the number of BGO elements that fired) which are dependent on the number of evaporated particles. Gamma-gamma coincidences were collected with the HPGe detectors and correlation arrays were formed for each reaction, with the condition that $K \geq 15$. The number of γ-γ coincidences in the matrices for the ^{37}Cl+^{113}Cd and the ^{37}Cl+^{114}Cd reactions totalled approximately 9×10^8 and 6×10^8, respectively. The identification of a set of mutually coincident γ rays belonging to ^{146}Tb was then possible; the transitions were 390, 591, 706, and 818 keV (and have not been identified prior to this study). Also, a set of mutually coincident γ rays belonging to ^{147}Tb [68] was confirmed; namely 405, 697, 772, and 1266 keV. Lists were formed with the four γ rays associated with ^{146}Tb and with those associated with ^{147}Tb.

In replaying the particle-vetoed (mainly the neutron exit channels) GASP data, cuts of $K \geq 10$ and $K \geq 20$ were made. With the gate lists given above, γ-ray spectra were obtained for the most intensely populated structures in ^{146}Tb and ^{147}Tb by summing the appropriate combinations of the two-dimensional energy windows set on three-fold coincidence events and the intensities of the 818 keV line in ^{146}Tb and

of the 697 keV line in ^{147}Tb were measured. Relative to the 818 keV line in ^{146}Tb, the intensity of the new superdeformed band was found to increase by a factor of about 5 between the data sets corresponding to the cuts $K \geq 10$ and $K \geq 20$ yet relative to the 697 keV line in ^{147}Tb, the superdeformed band intensity was found to be independent of the K-cut. Given that K distributions for normally deformed and superdeformed states are normally very similar [58], the ratio of the superdeformed band intensity in a given residual nucleus relative to normally deformed states in that same nucleus should be nearly independent of the K-cut. For this reason the new band, shown in figure 5.1, was assigned to the nucleus ^{147}Tb. The intensity of the band was determined to be approximately 0.4% relative to the 4n exit channel. In comparison, optimum values typically measured for other yrast superdeformed bands in the $A \sim 150$ mass region are about 1%.

Total Routhian Surface (TRS) calculations were performed for ^{147}Tb and particle configurations were studied. The TRS for the (parity, signature) configuration of $(\pi, \alpha) = (-, +1/2)$ in ^{147}Tb is shown in figure 5.2. In these calculations, neutron and proton configurations were fixed to $(\pi, \alpha) = (-, 0)$ and $(\pi, \alpha) = (+, +1/2)$, respectively. Evidence of a superdeformed minimum located at $(\beta_2, \beta_4, \gamma) = (0.54, 0.07, 2.3°)$ is clear. The TRS plotted corresponds to a value of $\hbar\omega \sim 0.7$ MeV and the superdeformed band in ^{147}Tb is predicted to become yrast between $I \sim 50\hbar$ and $I \sim 65\hbar$. Shown in figure 5.3 is the proton single-particle Routhians for ^{147}Tb generated from Cranked Shell Model (CSM) calculations [21] with a Woods-Saxon potential, the deformation parameters being fixed to those of the minimum seen in the TRS. The proton single-particle Routhians suggest that, for the yrast configuration, the 6_3[†] intruder orbital should be occupied in the feeding region above $\hbar\omega \sim 0.5$ MeV. There-

[†]The 6_3 label corresponds to the Nilsson quantum number $[651]\frac{3}{2}^+$. Also, the 6_1 and 6_2 labels correspond to signature partners with the Nilsson quantum number $[660]\frac{1}{2}^+$.

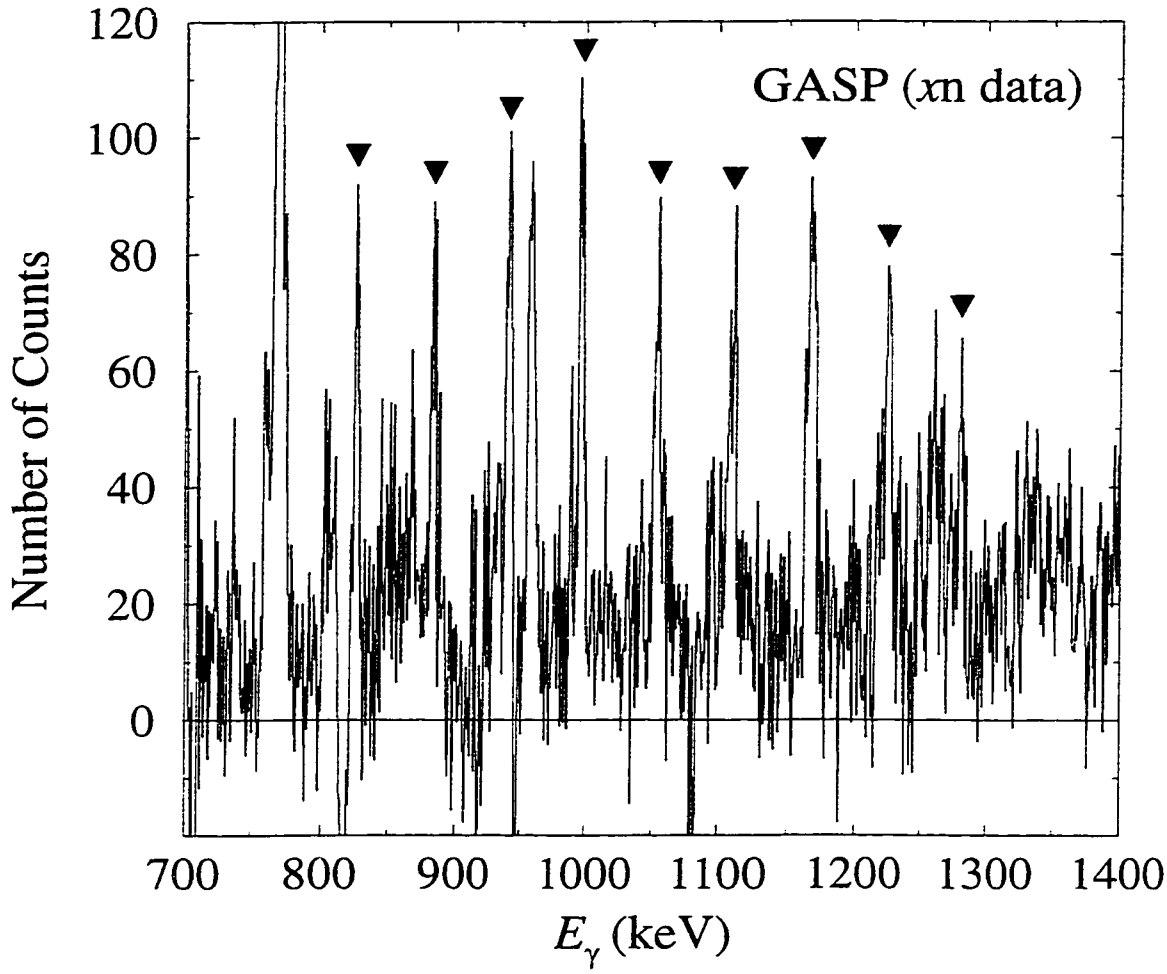

Figure 5.1: The superdeformed band that has been assigned to ^{147}Tb. The partial γ-ray spectrum was obtained by summing all combinations of two-dimensional energy windows set on three-fold coincidence events and a small fraction of the single-gated spectrum was used for the background subtraction. The energies of the nine transitions marked by the inverted triangles are 826, 884, 941, 998, 1055, 1111, 1167, 1224, and 1281 keV.

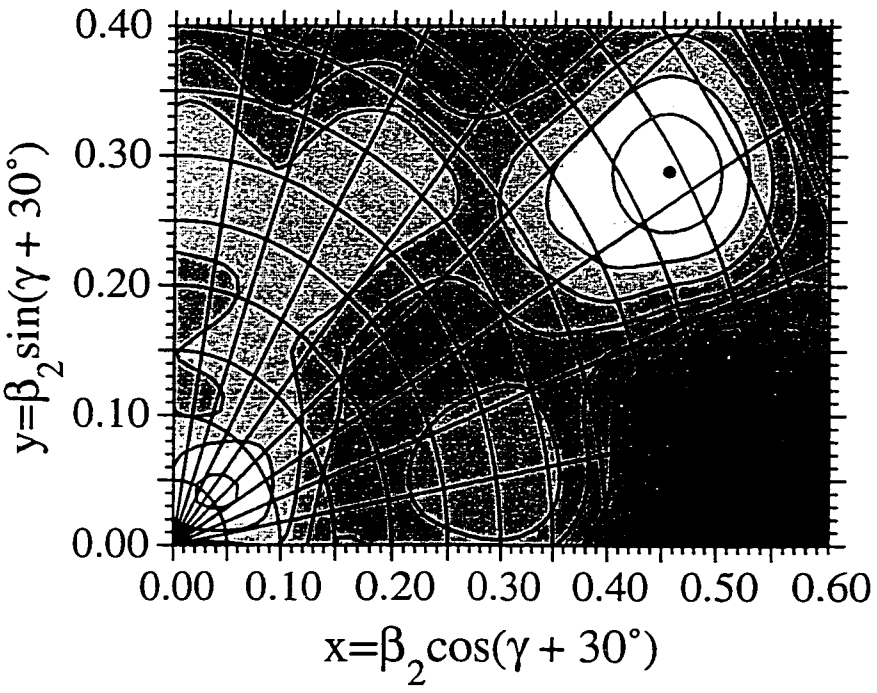

Figure 5.2: TRS for the $(\pi, \alpha) = (-, +1/2)$ configuration in ^{147}Tb showing evidence of a superdeformed minimum located at $(\beta_2, \beta_4, \gamma) = (0.54, 0.07, 2.3°)$. This TRS corresponds to a rotational frequency of $\hbar\omega \sim 0.7$ MeV. The superdeformed band in ^{147}Tb is predicted to become yrast between $I \sim 50\hbar$ and $I \sim 65\hbar$.

fore, the proton (π) intruder configuration of ^{147}Tb may be assumed to be $\pi 6^3$, which means that the first three $N = 6$ proton intruder orbitals are occupied, as opposed to the configuration $\pi 6^1 \otimes [404]^2_{9/2^+}$[†] observed in ^{145}Tb.

To assign the neutron configuration of the ^{147}Tb superdeformed band the $\mathcal{J}^{(2)}$ moment of inertia was considered. The $\mathcal{J}^{(2)}$ moments of inertia calculated from γ-ray transitions of superdeformed bands in ^{146}Gd [66] and ^{147}Tb are shown in figure 5.4. The peak in the $\mathcal{J}^{(2)}$ of ^{146}Gd(a), due to the crossing of two $N = 6$ neutron orbitals [58], is not observed for either ^{146}Gd(b) or ^{147}Tb. Therefore, the neutron (ν) intruder configuration of ^{147}Tb is most likely the same as that of ^{146}Gd(b) and the

[†]The label $\pi 6^1 \otimes [404]^2_{9/2^+}$ means that one proton is in the $N = 6$ intruder orbital and two protons are in the $[404]^{9/2^+}$ orbital.

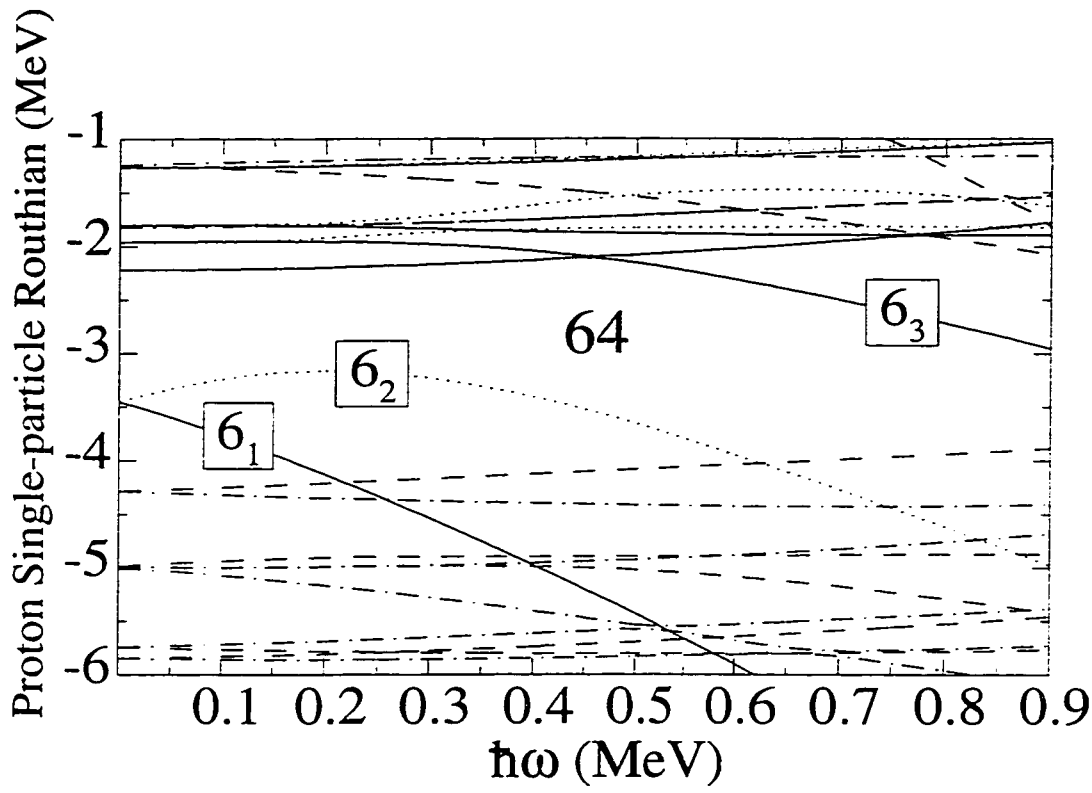

Figure 5.3: Proton single-particle Routhians for ^{147}Tb generated from CSM calculations based on the Woods-Saxon potential. The intruder orbitals 6_1, 6_2, and 6_3 and the particle number that corresponds to the energy gap have been labeled. Solid lines correspond to parity signature $(\pi, \alpha) = (+, +1/2)$, dotted lines to $(+, -1/2)$, dashed lines to $(-, -1/2)$, and dot-dashed lines to $(-, +1/2)$.

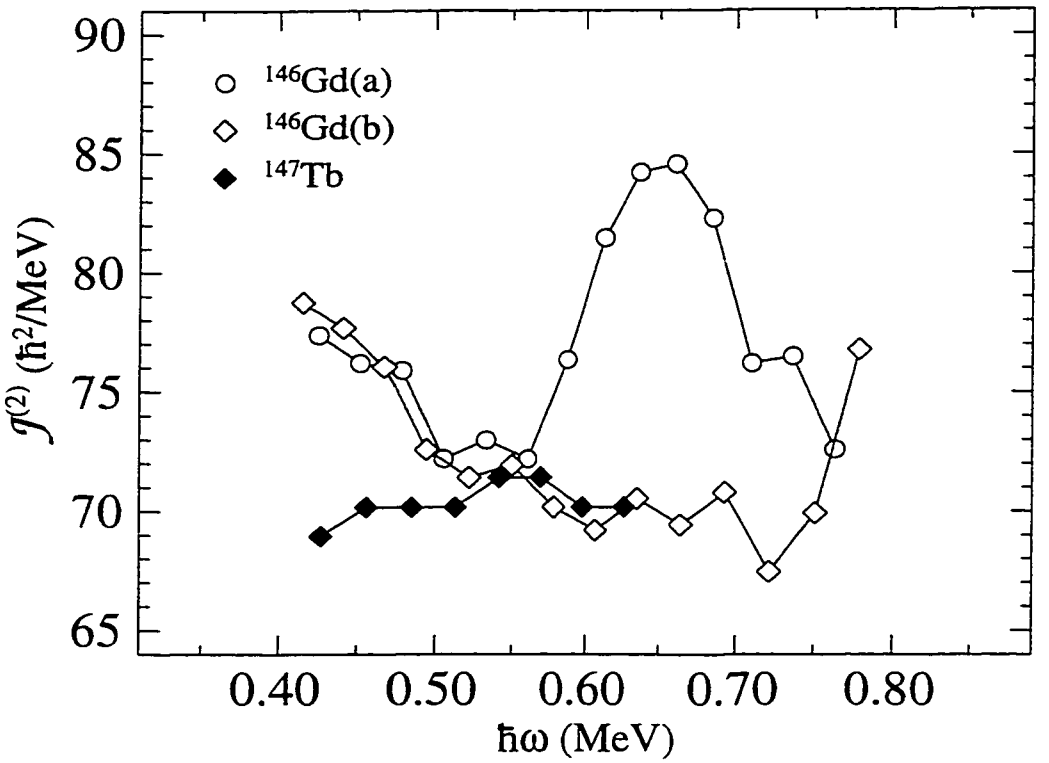

Figure 5.4: Experimental $\mathcal{J}^{(2)}$ moments of inertia for ^{146}Gd(a), ^{146}Gd(b), and ^{147}Tb.

configuration is assigned as $\nu 7^1$, which means that one $N = 7$ neutron intruder orbital is occupied. The signature partner of the new band, corresponding to the neutron configuration of ^{146}Gd(a), should be populated with similar intensity but was not discovered in the present work.

5.3 Summary

A new superdeformed band has been found and assigned to the nucleus ^{147}Tb. This is the first superdeformed band to have been found in ^{147}Tb. The proton intruder configuration is suggested to be $\pi 6^3$, like that of the heavier terbium isotopes and unlike that of ^{145}Tb, and $\mathcal{J}^{(2)}$ moment of inertia suggests that the neutron intruder configuration of ^{147}Tb is probably $\nu 7^1$. Therefore, the band configuration is assigned

as $\pi 6^3 \nu 7^1$ with a total parity and signature of $(\pi, \alpha) = (-, +1/2)$.

Chapter 6

Enhancement of Superdeformed Band Population in ^{135}Nd

"Everything has been thought of before,
but the problem is to think of it again."

Johann W. von Goethe (1749-1832) [34]

Up to this point the material that has been presented has focused on providing a clear description of the phenomenon of superdeformation. However, as mentioned in the introductory chapter, the main focus of this Thesis is not only to discuss superdeformation but to use it as a tool to study fusion-evaporation reactions. Over the past few years much work has been done on so-called entrance-channel effects in the mass $A \sim 150$ region (see for example [69, 70, 71, 72]). Specifically, mass-symmetric reactions have been noted to enhance the population of superdeformed states compared to mass-asymmetric reactions forming the same compound nucleus at the same excitation energy. These enhancements are, however, not fully understood. In this chapter it is shown that enhancement of superdeformed band population in ^{135}Nd results from a modification of the compound-nucleus angular-momentum distribution due to the presence of low-lying vibrational states in the target/projectile

nuclei. Much of the material presented in this chapter has been published in *Physical Review Letters* [3] and in *Journal of Physics G* [73].

6.1 The History of "Entrance-Channel Effects"

It has been observed that the population of superdeformed bands in the mass $A \sim 150$ region is enhanced for mass-symmetric fusion-evaporation reactions [69, 70]. No such effects have been measured for superdeformed rotational bands in nuclei with mass $A \sim 130$ [74, 75] and $A \sim 190$ [76, 77]. Smith *et al.* [69] suggested that, in the mass $A \sim 150$ region, entrance-channel effects associated with an increase of the fusion time for mass-symmetric reactions, as compared to mass-asymmetric reactions, were responsible for the observed enhancements. In other words, neutron emission could compete more favorably with fission thus increasing the maximum angular momentum leading to evaporation residues and subsequently resulting in a higher probability of decay into superdeformed states. However, dissipative collision calculations performed [75] with the code HICOL predicted extremely small differences in the fusion times of the compound nucleus ^{156}Dy formed with the reactions studied by Smith *et al.*. Moreover, measurements of the γ-ray decay of giant dipole resonances suggested that no increases in the fusion time existed in the formation of the compound nucleus ^{146}Gd [78]. This suggests that the feeding enhancement of superdeformed bands is not an entrance-channel effect associated with increased fusion time for mass-symmetric reactions and alternative explanations should be investigated.

The possible existence of entrance-channel effects in the decay of a compound nucleus has been investigated in the past and it is worthwhile to briefly review the work that has been done on the subject. One of the first studies to suggest the presence of entrance-channel effect was performed by Kühn *et al.* [79]. Neutron mul-

tiplicities measured for the nearly mass-symmetric reaction ^{64}Ni+^{92}Zr were found to be drastically overestimated by statistical-model calculations. It was suggested that this was due to trapping in a superdeformed minimum and that the neutron multiplicity for a given spin interval should depend on the mass asymmetry of the entrance channel. A later study by Janssens *et al.* [80] concerned similar measurements of neutron multiplicities for the reactions ^{64}Ni+^{92}Zr and ^{12}C+^{144}Sm. An agreement between statistical-model calculations and experimental measurements of the neutron multiplicities was reported for the mass-asymmetric reaction but not for the mass-symmetric reaction. With the same two reactions, Ruckelshausen *et al.* [81] measured the ratio of 2n to 3n cross sections as a function of compound-nucleus spin. In that particular study it was noted that the ^{64}Ni-induced reaction evaporated fewer neutrons. The interpretation of the results for the latter two studies followed that given by [79].

It is well known that fusion-barrier fluctuations [82] broaden the compound-nucleus spin distribution [41, 46, 83] (see section 4.2), thus resulting in an increase of the rotational energy and a reduction in effective temperature of the compound nucleus. It was soon realized that such fluctuations might provide an alternative explanation for the reduction of the neutron-evaporation probability noted to occur in mass-symmetric reactions. For example, Haas *et al.* [84] concluded that nuclear-shape vibrations were necessary to explain measured γ-ray multiplicities of individual exit channels for more mass-symmetric reactions and that, near the barrier, the average angular momentum transferred greatly depends on the mass-asymmetry of the entrance channel. Also, Love *et al.* [85] were able to explain the observed neutron multiplicity for the reaction ^{64}Ni+^{92}Zr with calculations that incorporated coupling to inelastic channels. By studying the feeding pattern of collective states they were

also able to conclude that trapping in superdeformed states at low spin did not occur.

Recently, Barreto *et al.* [86] readdressed the discrepancies between the above two interpretations. The decay of the compound nucleus ^{164}Yb, formed in the reactions ^{64}Ni+^{100}Mo and ^{16}O+^{148}Sm, was examined and it was found that γ-ray fold distributions of the various evaporation channels showed differences depending on the entrance channel. The results were consistent with fusion models that predict an increase in the width of the compound-nucleus spin distribution in the ^{64}Ni-induced reaction.

6.2 Motivation for this Study

The work presented in this chapter establishes a relationship between the enhancement of superdeformed band population and the modification of the compound-nucleus spin distribution due to the presence of low-lying vibrational states in the target/projectile nuclei. The so-called entrance-channel effects observed in the mass $A \sim 150$ region could possibly be explained by this phenomenon. In order to compare any two reactions, their excitation energies should be matched as closely as possible. It is equally important that the uncoupled spin distributions, i.e. fusion cross sections when no coupling to low-lying vibrational states is included, be matched for the two reactions. For the reactions leading to the population of superdeformed bands in the $A \sim 150$ mass region such a matching usually occurs at very high angular momenta where the fission process begins to compete with the formation of evaporation residues. Unfortunately, little is known about the height of the fission barrier and its spin dependency for compound nuclei produced at extremely high angular momenta. However, superdeformed bands in the mass $A \sim 130$ region become yrast at relatively low spins and they can therefore be populated by fusion reactions for which the fission

probability is negligibly small.

For a first study, the search for coupled-channel effects can be simplified by investigating a superdeformed band in a nucleus around $A = 130$. Furthermore, linking transitions between superdeformed and normally deformed states have been observed in many cases and therefore experimental spin assignments have been performed for a number of superdeformed bands in this mass region. Reactions ideally suited for this particular study were ^{74}Ge+^{64}Ni and ^{26}Mg+^{112}Cd forming the compound nucleus ^{138}Nd with excitation energies of 50.5 and 50.7 MeV, respectively.

Shown in figure 6.1 are theoretical fusion cross sections as a function of the compound-nucleus spin calculated with the code CCFUS. The accepted deformation parameters, β_λ, for the first 2^+ and 3^- excited states of ^{74}Ge, ^{64}Ni, ^{26}Mg, and ^{112}Cd (see table 4.1) were used as inputs to CCFUS. Target thicknesses (see section 6.3) were taken into account for all calculations by integrating over the appropriate energy spreads. The upper panel of the figure presents the cross sections when no coupling to low-lying vibrational states are included in the calculations, illustrating the closely matched spin distributions. Having similar uncoupled spin distributions is essential for the present investigation. The lower panel gives the cross sections when coupled channels are taken into account, showing a $10\hbar$ increase in spin for the ^{74}Ge-induced reaction.

6.3 Experimental Setup

As mentioned above, the reactions ^{74}Ge+^{64}Ni and ^{26}Mg+^{112}Cd were studied at bombarding energies of 239 and 94 MeV, respectively, with the nucleus ^{135}Nd being populated through the 3n exit channel. The ^{64}Ni and ^{112}Cd targets consisted of foils of $\sim$380 and $\sim$500 μg/cm^2, respectively; the loss of beam energy through the targets was

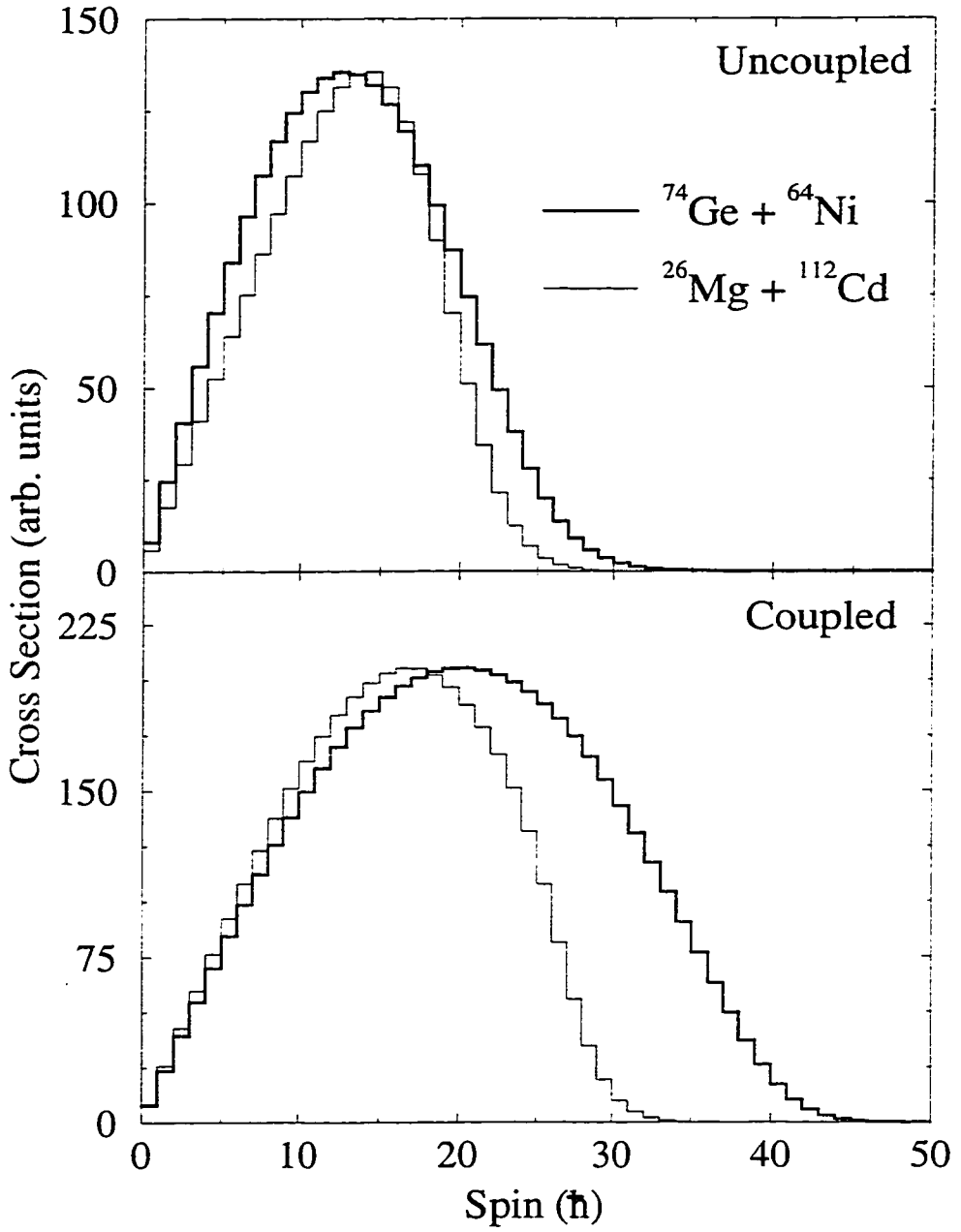

Figure 6.1: Calculated compound-nucleus spin distributions. Upper panel: spin distributions when no coupling to low-lying vibrational states are included in the calculations. Lower panel: spin distributions when coupled channels are taken into consideration. Target thicknesses (see section 6.3) were taken into account in the calculations and the curves were normalized at their maxima for each panel.

about 8 MeV for the ^{74}Ge-induced reaction and about 2 MeV for the ^{26}Mg-induced reaction. Thus, the excitation energy of the compound nucleus ^{138}Nd was $E^* = 50.5$ MeV (at mid target) for the mass-symmetric reaction and $E^* = 50.7$ MeV (at mid target) for the mass-asymmetric reaction. The appropriate beams were provided by the TASCC facility and γ rays emitted by the de-exciting nuclei were detected with the 8π Spectrometer. In order for an event to be recorded on tape, two or more HPGe detectors and three or more BGO elements had to fire in prompt time coincidence. A total of 19×10^6 and 11×10^6 γ-γ coincidences were collected for the ^{74}Ge+^{64}Ni and ^{26}Mg+^{112}Cd reactions, respectively.

6.4 Data Analysis and Results

As a first step in the analysis of the data collected, K distributions were extracted for each reaction, where K is the number of BGO elements that fired for a single event. This was done by double gating on the appropriate lists of γ rays, i.e. histograming only those K values for which two members in a given list where in coincidence, given in table 6.1.

Presented in figure 6.2 are the K distributions for exit channels leading to the residual nuclei ^{134}Nd, ^{135}Nd, and ^{136}Nd. For comparison, the K distribution for superdeformed states in ^{135}Nd [88, 90] is also shown. A large centroid shift between the two reactions is evident for the 2n channel and becomes less apparent when the neutron multiplicity increases; this feature has been noted in earlier studies [81, 84, 86]. It should also be pointed out that similar centroid shifts have been reported for other superdeformed bands [75, 77]. Figure 6.3 gives weighted sums of the K distributions, corresponding to normally deformed states in the individual xn channels, shown in the previous figure. The larger centroid and high-K tail seen for the ^{74}Ge+^{64}Ni re-

Table 6.1: Lists of γ rays used to obtain the K distributions shown in figure 6.2.

Residual nucleus [Ref.]	E_γ (keV)	$I_i^{\pi_i} \rightarrow I_f^{\pi_f}$
^{134}Nd [87]	295	$2^+ \rightarrow 0^+$
	495	$4^+ \rightarrow 2^+$
	632	$6^+ \rightarrow 4^+$
^{135}Nd [88]	199	$\frac{11}{2}^- \rightarrow \frac{9}{2}^-$
	595	$\frac{15}{2}^- \rightarrow \frac{11}{2}^-$
	728	$\frac{19}{2}^- \rightarrow \frac{15}{2}^-$
^{136}Nd [89]	374	$2^+ \rightarrow 0^+$
	603	$4^+ \rightarrow 2^+$
	771	$6^+ \rightarrow 4^+$

action are indicative of the fact that higher spins were reached in that reaction when compared to the ^{26}Mg+^{112}Cd reaction.

To gain an understanding of coupled-channel effects at relatively high spin, nuclei exhibiting discrete superdeformed states may be studied. Shown in figure 6.4 are background-subtracted coincidence spectra for the superdeformed band in ^{135}Nd, for the two reactions, obtained by summing clean coincidences. As predicted by coupled-channel calculations, the superdeformed band is seen to higher spin in the ^{74}Ge-induced reaction than in the ^{26}Mg-induced reaction. More precisely, the band is seen up to the 1147 keV $32.5\hbar \rightarrow 30.5\hbar$ transition for the former reaction, whereas the last discernible transition for the latter reaction is 1011 keV $28.5\hbar \rightarrow 26.5\hbar$.

One could try to unfold the above K distributions in order to obtain experimental spin distributions. However, such an unfolding procedure would generate large uncertainties and it is much easier to study the population of discrete states.

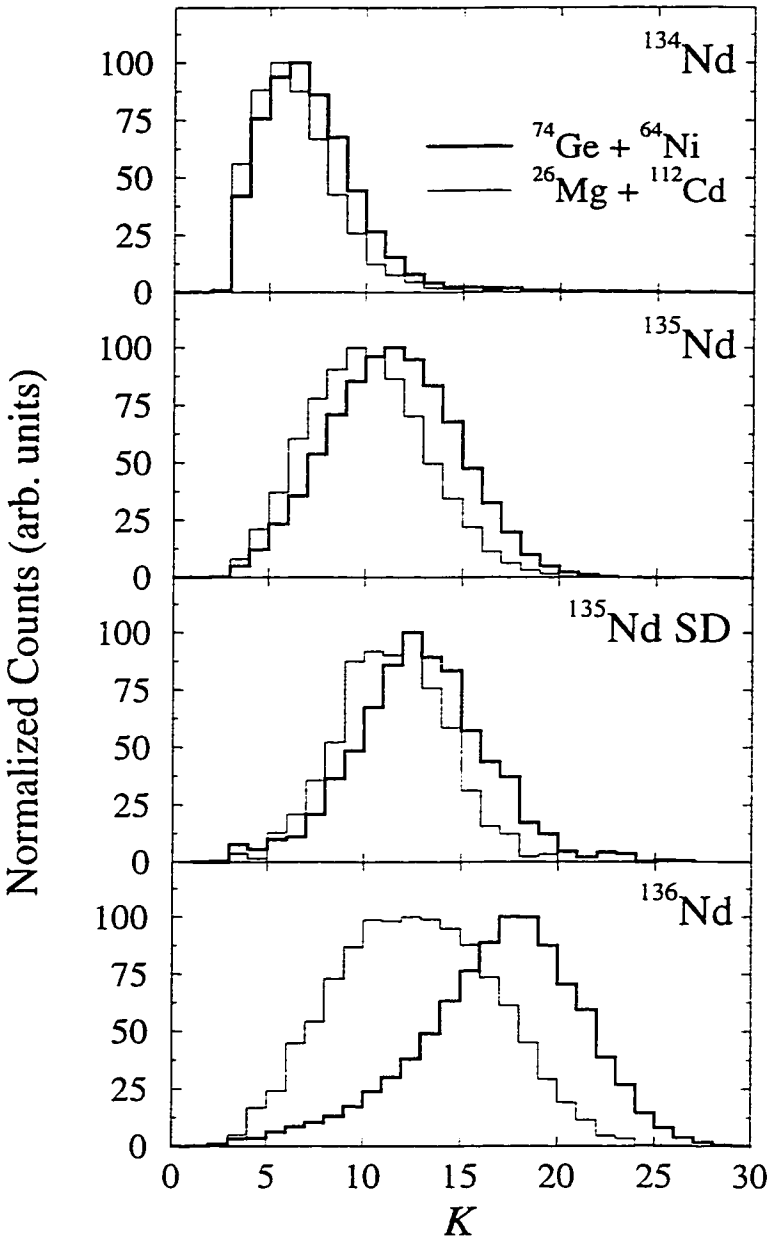

Figure 6.2: Total number of firing BGO elements, K, measured for the individual xn channels. Shown are the K distributions corresponding to transitions between normally deformed states in ^{134}Nd, ^{135}Nd, and ^{136}Nd and for superdeformed states in ^{135}Nd. All distributions have been normalized to 100 at their maximum.

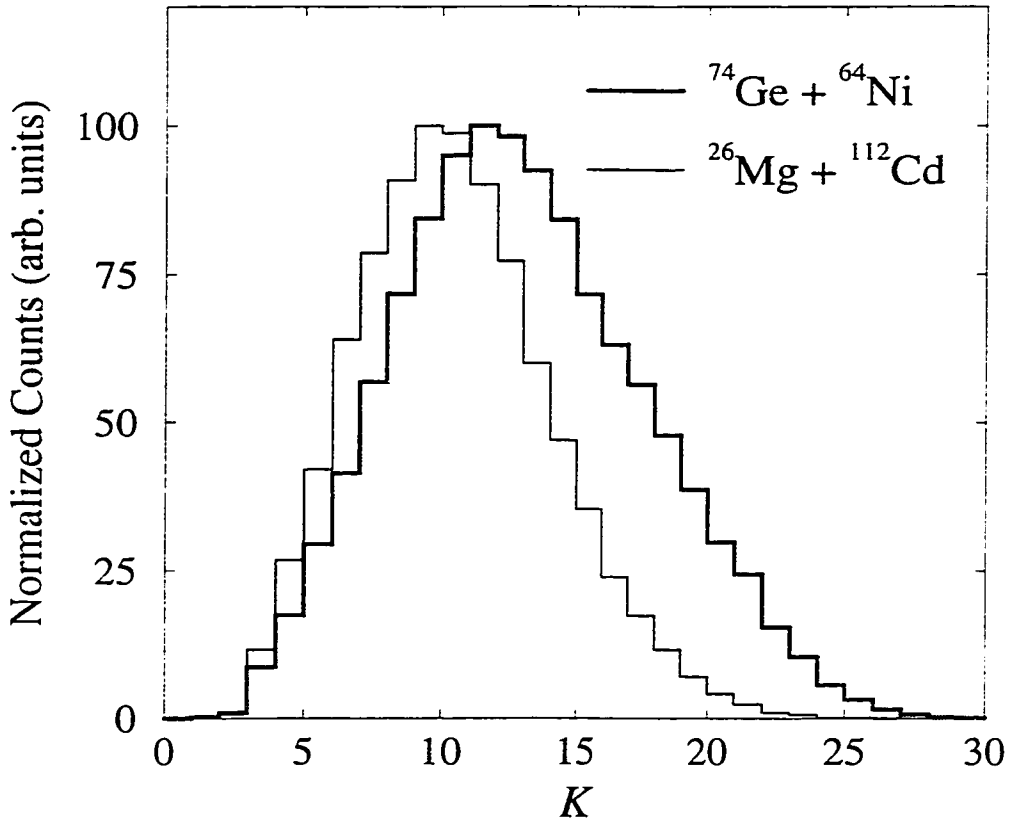

Figure 6.3: Total number of firing BGO elements, K, measured for the xn channels for the two reactions studied. These spectra correspond to weighted sums of the K distributions, corresponding to normally deformed states in the individual xn channels, shown in the previous figure. Measured cross sections for the xn channels (see table 6.2) were used in the weighting procedures. Each distributions has been normalized to 100 at its maximum.

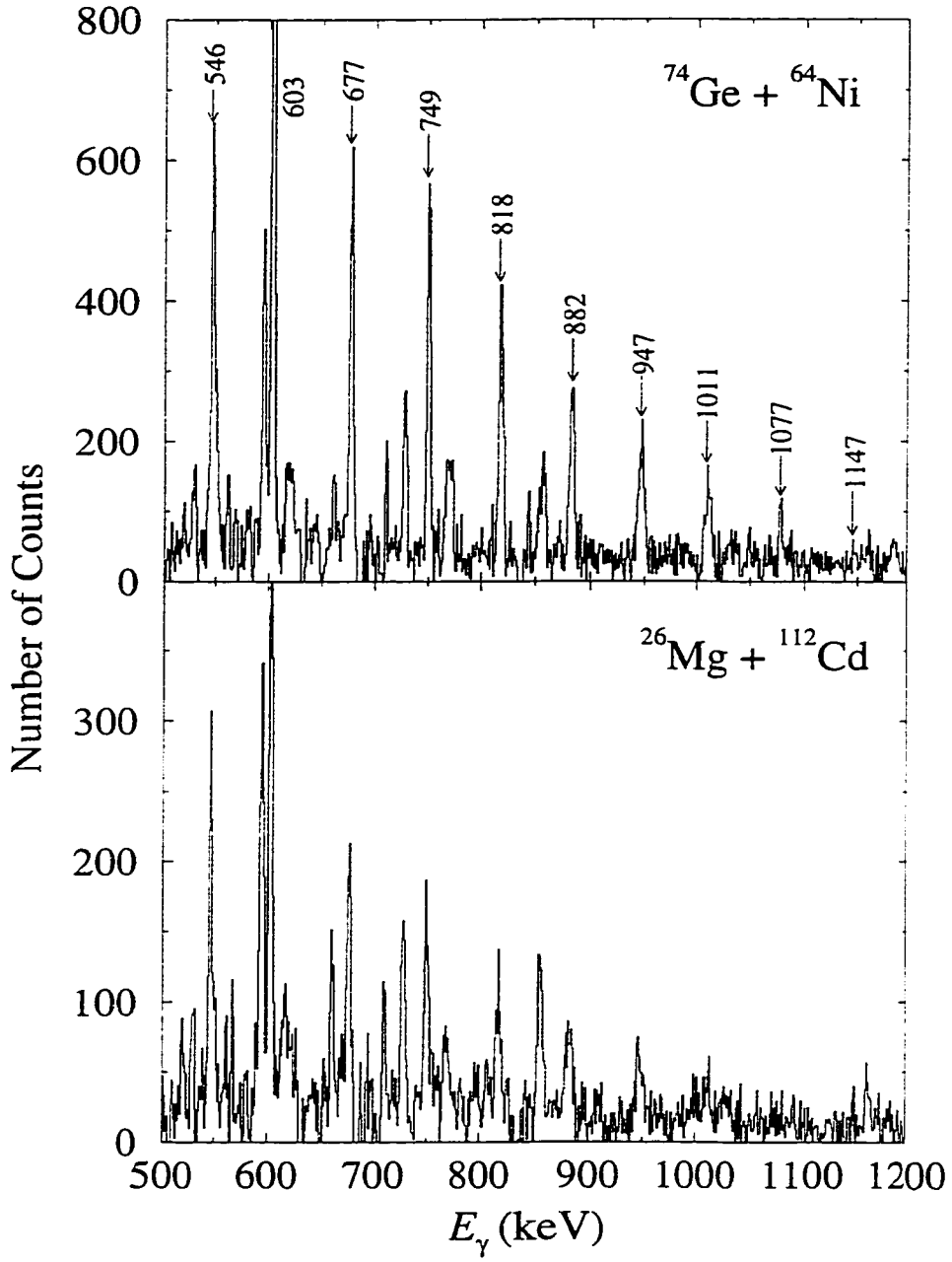

Figure 6.4: Partial coincidence spectra for the superdeformed band in ^{135}Nd for the two reactions studied. In both cases the spectra were obtained by summing coincidences of the 546, 677, 749, 818, 882, 947, 1011, 1077, and 1147 keV lines. A small fraction of the total projection, of the appropriate γ-γ coincidence matrix, was used to subtract background for each reaction.

To do this a ratio of intensities is defined

$$R = \frac{\mathcal{I}^I(\mathrm{Mg} + \mathrm{Cd})}{\mathcal{I}^I(\mathrm{Ge} + \mathrm{Ni})} \tag{6.1}$$

where $\mathcal{I}^I$ is the intensity of a given γ-ray transition measured for the stated reaction and I is the spin of the state emitting that γ ray. Shown in figure 6.5 is a plot of R versus spin I. It should be pointed out that the intensities of the lowest spins measured, for the various exit channels, have been normalized to unity for each reaction. Intensities were obtained with the data analysis program ESCL8R [63]. The difference in the population of high-spin states between the two reactions is quite remarkable. At spin $16.5\hbar$, for example, the enhancement of the ^{74}Ge-induced reaction relative to the ^{26}Mg-induced reaction (i.e. $1/R$) is equal to about 2 while at spin $26.5\hbar$ the enhancement is considerably larger having a value of ~ 20. It should be noted that this is the first reported case of any sort of enhancement to be measured as a function of spin for superdeformed states.

The theoretical spin distributions, shown in figure 6.1, were used as inputs to the code evapOR. With the level density formalism of Gilbert and Cameron and a level density parameter of $a = A/9.0$ MeV^{-1}, cross sections of various exit channels were calculated and compared to values extracted from experiment (see table 6.2). It is clear that the inclusion of coupled-channels is necessary in order to reproduce the experimental measurements. Two different level density parameters are usually used in statistical codes when modelling the population of normally deformed and superdeformed states (see for example [91, 92]). This level density difference is however known to mainly influence the statistical spectra and most likely does not affect the enhancement of interest here.

With the coupled spin distributions as input to evapOR entry-spin, i.e. the spin of the state emitting the first γ ray immediately following particle evaporation

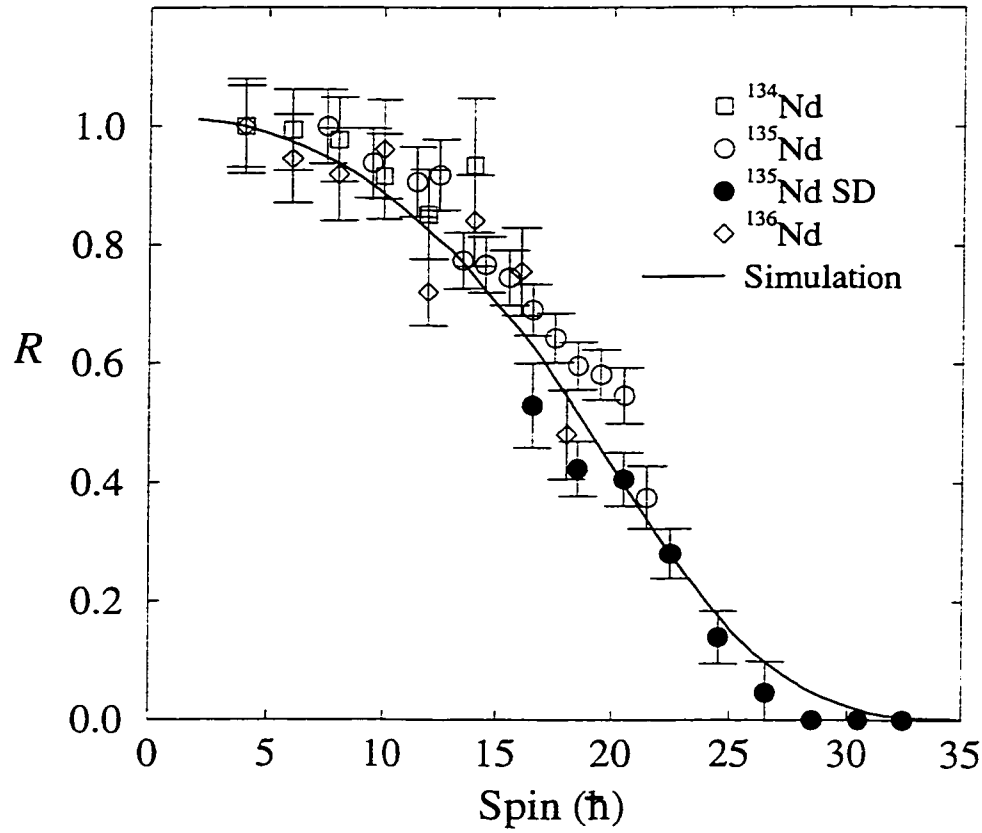

Figure 6.5: The ratio of intensities R, see text for details, as a function of spin, where spin refers to the state emitting a given γ ray. The smooth solid line is a theoretical simulation done with the code evapOR. The coupled spin distributions calculated with CCFUS were used as inputs to the statistical code.

for nuclei surviving fission, distributions were calculated. The results are shown in figure 6.6. A theoretical value for R as a function of I was then calculated using the theoretical entry-spin distributions and is represented as the solid curve (normalized to unity at spin $4\hbar$) in figure 6.5. The agreement between theory and experiment is excellent. However, it should be pointed out that the code CCFUS is a relatively simple approach to the coupled-channel problem and more refined calculations should probably be performed for the systems investigated in the present work. It is interesting to note that the theoretical enhancement compares equally well to the trend seen

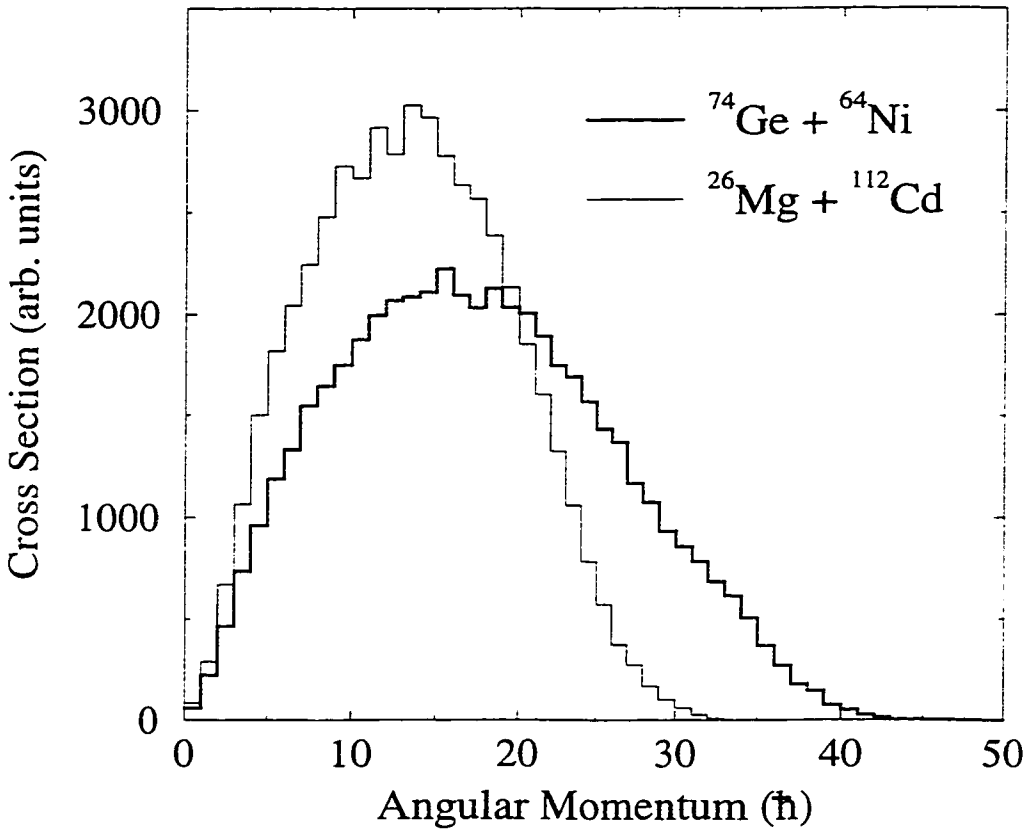

Figure 6.6: Calculated total cross section of all events surviving fission as a function of entry spin for the two reactions studied. Note that the two curves have been normalized such that the total cross section (total area under each curve) is the same for each reaction.

Table 6.2: Measured and calculated relative cross sections (C.S.) for the various channels observed. Note that the cross section for the 3n channel has been normalized to unity. All experimental uncertainties are within one percent of the stated relative cross section.

Reaction	Residual nucleus	Exp. C.S.	Calc. C.S. (uncoupled)	Calc. C.S. (coupled)
$^{74}Ge+^{64}Ni$	^{135}Nd	1.00	1.00	1.00
	^{136}Nd	0.45	0.13	0.45
	^{134}Nd	0.08	0.21	0.11
	^{132}Ce	0.11	0.18	0.17
$^{26}Mg+^{112}Cd$	^{135}Nd	1.00	1.00	1.00
	^{136}Nd	0.25	0.10	0.17
	^{134}Nd	0.09	0.21	0.15
	^{132}Ce	0.12	0.17	0.16

for superdeformed states in ^{135}Nd as it does to the trend seen for normally deformed states. This is an indication that the trend in the enhancement is purely a spin effect and that a time delay in the fusion of the mass-symmetric system probably does not occur.

6.5 Summary

It has been proposed that the differences in superdeformed band population observed in recent experiments result from a modification of the compound-nucleus angular-momentum distribution due to the presence of low-lying vibrational states in the target/projectile nuclei. To test this hypothesis the nucleus ^{135}Nd was studied with the reactions $^{74}Ge+^{64}Ni$ at 239 MeV and $^{26}Mg+^{112}Cd$ at 94 MeV. The uncoupled spin distribution and excitation energy of the compound nucleus ^{138}Nd were closely matched for the two reactions. Of the two reactions, the ^{74}Ge-induced reaction was found to preferentially populate high-spin states, including superdeformed states.

This is the first report of such an effect in the mass $A \sim 130$ region and the first time that such measurements have been made for discrete superdeformed states as a function of spin. The results are consistent with coupled-channel calculations that predict a broadening of the compound-nucleus spin distribution for the mass-symmetric reaction. A similar explanation may be applicable to the enhancement observed for superdeformed states in the mass $A \sim 150$ region. However, the situation is more complex in the mass $A \sim 150$ region due to the competition between fission and particle evaporation at high spin and more experimental work is needed. In particular, it would be important to obtain reliable feeding patterns of superdeformed bands for the reactions where population enhancements have been observed. Such a study, which can only be done with γ-ray spectrometers of the third generation (like GammaSphere), will be presented in the next chapter.

Chapter 7

Population of Superdeformed Bands at Extreme Angular Momenta

" 'But, alas,' the Director shook his head,
'we can't bokanovskify indefinitely.' "

Aldous Huxley (1894-1963)
Brave New World [93]

In the previous chapter enhancement of superdeformed band population in the nucleus ^{135}Nd was observed for the mass-symmetric reaction ^{74}Ge+^{64}Ni compared to the mass-asymmetric reaction ^{26}Mg+^{112}Cd. The results were attributed to differences in compound-nucleus spin distributions brought on by coupling to inelastic channels in the fusion process. Although that particular study dealt with nuclei in the mass $A \sim 130$ region, where the fission of compound nuclei is negligible, the coupled-channel effects could also play a major role in the mass $A \sim 150$ region. The primary difference in the heavier mass region is that one would have to properly account for the competition between fission and particle evaporation. The present chapter attempts to establish a link between coupled-channel effects and observed increases (see section 6.1) in the population of high-spin states for mass-symmetric reactions

in the mass $A \sim 150$ region. Much of the material presented in this chapter has been accepted for publication in *Physical Review C* [4].

7.1 Motivation for this Study

Consider the reactions ^{76}Ge+^{76}Ge and ^{28}Si+^{124}Sn at bombarding energies of 323 and 152 MeV, respectively. Shown in the upper panel of figure 7.1 are coupled-channel spin distributions in the compound nucleus (histogram and left ordinate) calculated with the code CCFUS. In each case coupling to the first excited 2^+ quadrupole vibrational state and the first excited 3^- octupole vibrational state, see table 4.1, was taken into consideration for both the target and projectile nuclei. Also shown in the upper panel of the same figure (circles and right ordinate) are the fusion times for each system as a function of angular momentum, calculated with HICOL. For the average spin of each distribution, indicated by the vertical lines, one finds that the fusion times are approximately equal to 300×10^{-22} and 50×10^{-22} seconds for the mass-symmetric and mass-asymmetric reactions, respectively.

Entry-spin distributions were calculated with the code evapOR with the above-mentioned coupled-channel spin distributions as input to the code; recall that this particular combination worked extremely well in modelling the experimental results in chapter 6. The level density formalism of Gilbert and Cameron and a level density parameter of $a = A/8.0$ MeV^{-1} were employed. Also, the Sierk fission barrier [94] was used and the ratio of a at the saddle point to the ground-state value was set to unity [50]. The results of the calculations are shown in the lower panel of figure 7.1, normalized such that the cross section of all events occurring above $50\hbar$, taken here to represent the lowest spin feeding superdeformed states, is the same for each reaction. The predominant feature that one notices is the similarity of the two entry-spin

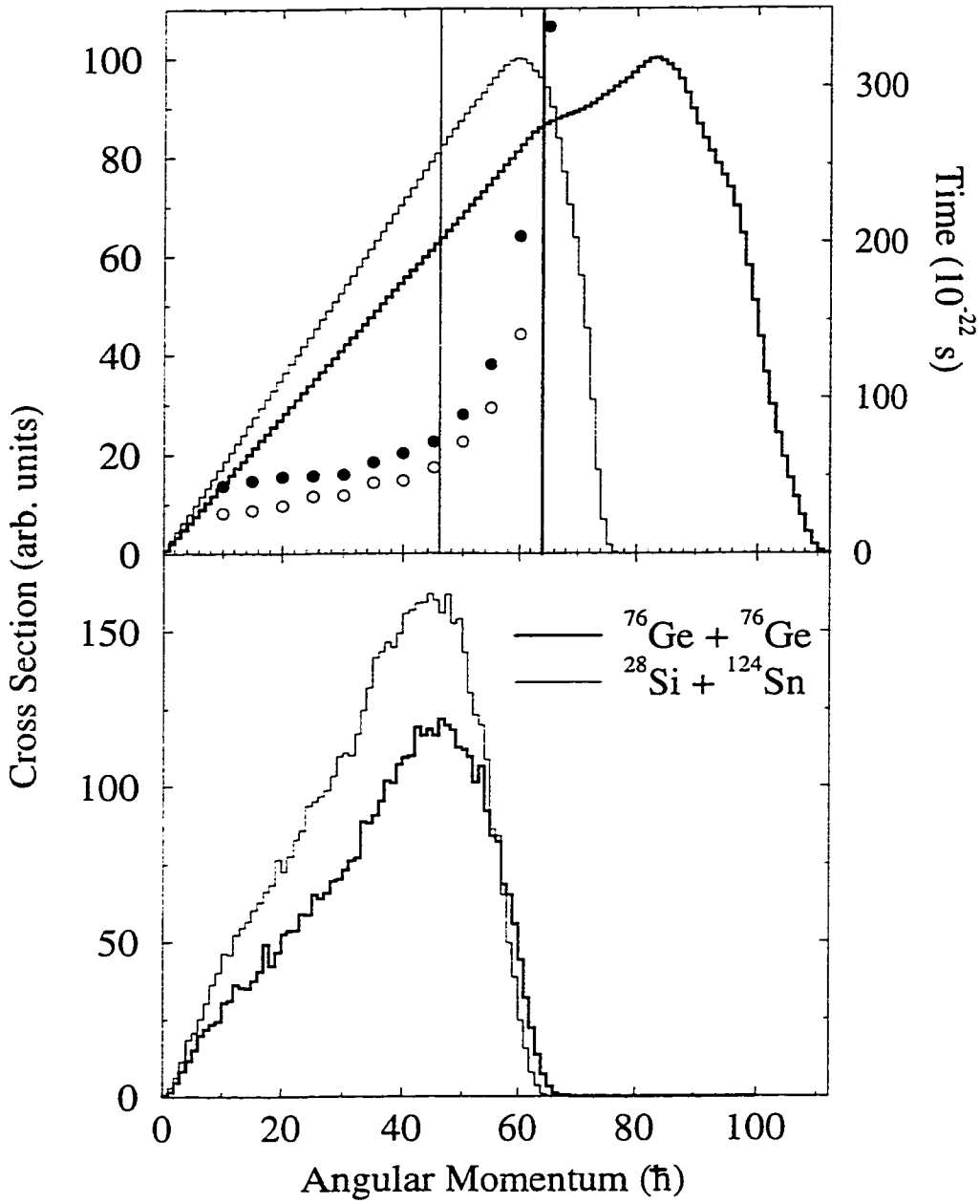

Figure 7.1: Upper panel (left ordinate): calculated compound-nucleus spin distributions. Target thicknesses (see section 7.2) were taken into account by integrating over the appropriate energy spreads. Note that the curves have been normalized to their maximum and that the vertical lines represent the average of each distribution. Upper panel (right ordinate): fusion times as a function of angular momentum for the ^{76}Ge-induced (filled circles) and ^{28}Si-induced (open circles) reactions. Lower panel: calculated total cross section of all events surviving fission as a function of entry spin for the two reactions studied, normalized such that the cross section of all events occuring above $50\hbar$ is the same for each reaction.

distributions, the mass-symmetric reaction losing much of the extra spin it had in its compound nucleus to fission. According to these calculations, for the production of the 5n evaporation channel (which corresponds to a favored channel for population of superdeformed states) an increase of only 13% is expected for the cross section above $50\hbar$, relative to the total cross section, for the mass-symmetric reaction. It should be pointed out, however, that the statistical calculations do not take into account dynamical effects in the fusion or fission processes.

The purpose of the work presented in this chapter is to measure the population of superdeformed states in gadolinium isotopes, formed with the above-mentioned mass-symmetric and mass-asymmetric reactions, to determine if the predicted similarity in the entry-spin distributions of the two reactions studied is indeed present. The gadolinium isotopes are ideal for such a study because the normally deformed and superdeformed structures which will be populated have been previously identified to very high spins and excitation energies.

7.2 Experimental Setup

The reactions ^{76}Ge+^{76}Ge and ^{28}Si+^{124}Sn were studied at bombarding energies of 323 and 152 MeV, respectively, with the nucleus ^{147}Gd being populated through the 5n exit channel. The ^{76}Ge target was a self-supporting foil of thickness 430 μg/cm^2 and the ^{124}Sn target consisted of two foils with thicknesses of 250 and 400 μg/cm^2; the loss of beam energy through the targets was 10 MeV for the ^{76}Ge-induced reaction and 4 MeV for the ^{28}Si-induced reaction. Thus, the excitation energy of the compound nucleus ^{152}Gd was $E^* = 87$ MeV (at mid target) for both reactions. The experiment was carried out with the GammaSphere multi-detector array. For this experiment GammaSphere was comprised of 97 HPGe detectors. A total of 5.5×10^8 and 1.7×10^8

events consisting of four or more coincident γ rays were collected for the ^{76}Ge-induced and ^{28}Si-induced reactions, respectively.

7.3 Data Analysis and Results

Shown in figure 7.2 are the γ-ray spectra obtained for the yrast superdeformed band in ^{147}Gd [58, 95] for the two reactions. These spectra were created, in accordance to reference [96], by triple gating on the band (i.e. histograming only those γ-ray energies in coincidence with at least three members of the superdeformed band) and the "spike-free" method [97] of spectrum incrementation was employed. Furthermore, uncorrelated background was minimized by ellipsoidal gating [98, 99, 100] and the backgrounds subtracted from the spectra were constructed according to the operator method of reference [101]. Details of background subtraction can also be found in reference [17].

The area under each of the peaks of the superdeformed band shown in figure 7.2 was measured and plotted as a function of assumed spin [102] to obtain peak-area profiles for each reaction, see figure 7.3. The average peak area in the plateau region, taken here to be represented by the bottom nine transitions of the band, was normalized to one for each reaction. The similarity of the peak-area profiles for the two reactions is obvious, however, a small difference is seen at high spin. The total intensity of the ^{147}Gd yrast superdeformed band was determined by averaging the peak areas of those transitions in the plateau region. In order to obtain an intensity measurement for normally deformed transitions in ^{147}Gd double gating on the 919, 373, and 809 keV lines, directly above the 550-ns isomer ($\frac{49}{2}^+$) [103], was performed. The intensities of the 919 and 373 keV lines, as well as the intensities of the 304, 239, and 618 keV lines occurring higher up in the level scheme, were measured. It

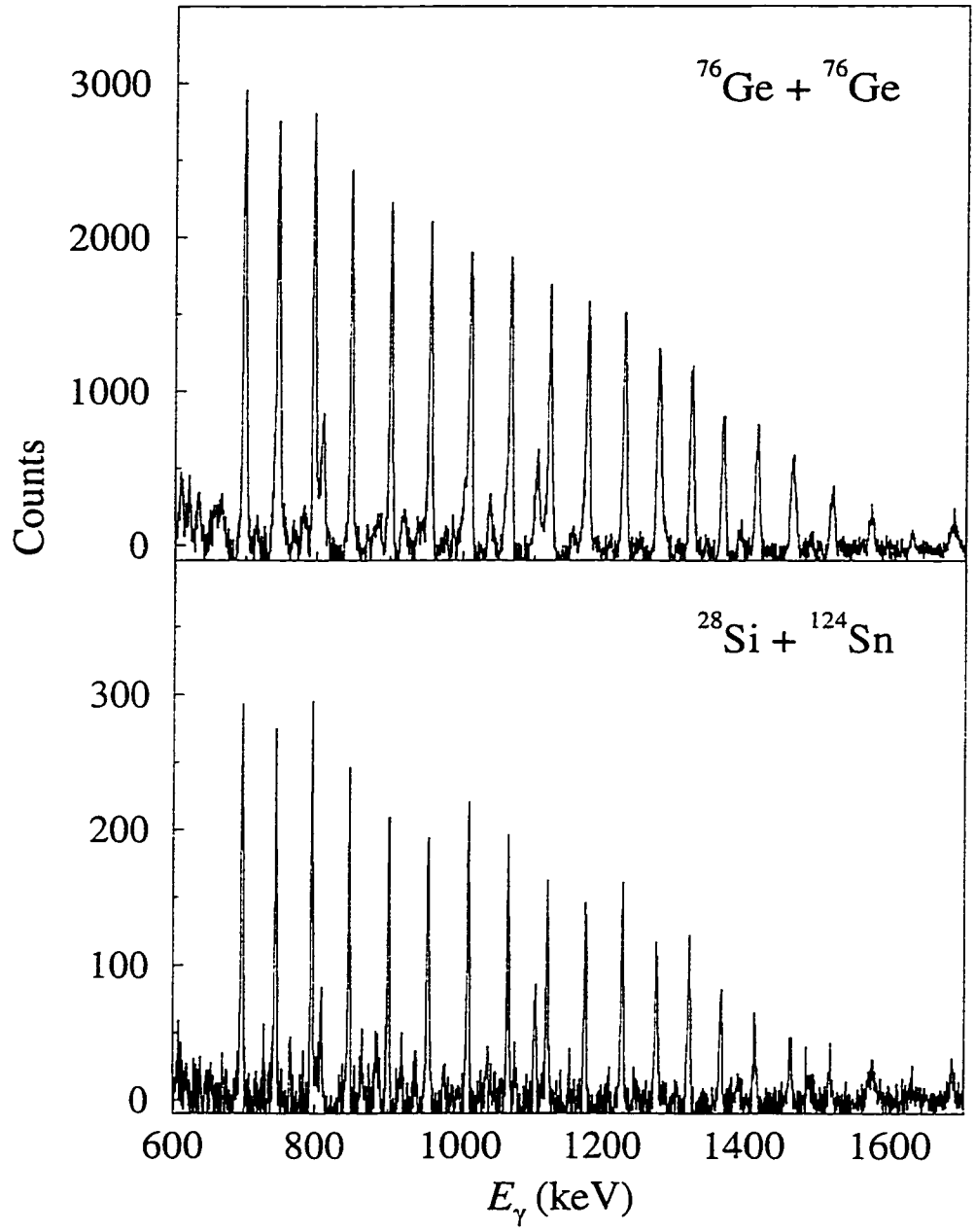

Figure 7.2: Portion of the triply-gated spectra for the yrast superdeformed band in ^{147}Gd for the two reactions studied. These spectra were obtained by setting gates on the bottom 17 transitions of the band.

should be noted that efficiency corrections were not required since ratios of intensities were extracted. Relative to normally deformed states, the band was found to be populated 4.6 ± 0.2 times more strongly for the mass-symmetric reaction compared to the mass-asymmetric reaction. Such a large ratio could not be explained by the statistical code used. Peak-area profiles for other superdeformed bands could not be extracted with confidence from the data set associated with the mass-asymmetric reaction due to insufficient statistics. This made a comparison of the two reactions extremely difficult for any of the other bands observed in the xn channels (i.e. yrast superdeformed bands in ^{146}Gd and ^{148}Gd and the first excited superdeformed band in ^{147}Gd). However, an estimated increase of about 4 to 5 times was extracted for the population of the yrast superdeformed band in ^{148}Gd [58, 65], for the mass-symmetric reaction in comparison with the mass-asymmetric reaction. It is therefore believed that the population increase of superdeformed states seems to be a general feature and is not limited to the yrast band in ^{147}Gd.

True relative intensity profiles for the yrast superdeformed band in ^{147}Gd were extracted by taking into account the effect of triple gating. An iterative fit was performed to the efficiency corrected peak-area profiles shown in figure 7.4, created by triple gating on the plateau region (the bottom nine transitions), with the following relation:

$$\mathcal{I}^{i}_{p.a.} = \sum_{(j<k<l)\neq i} \mathcal{I}_{t}^{max(i,j,k,l)} \tag{7.1}$$

Here j, k, and l are gate indices, i is a γ-ray index, and $\mathcal{I}^{i}_{p.a}$ are obtained from the peak-area profiles shown in figure 7.4. A Woods-Saxon function was assumed for the true intensity profile $\mathcal{I}_t$:

$$\mathcal{I}_t(I) = \frac{\mathrm{a_1}}{1 + \exp\left(\frac{I-\mathrm{a_2}}{\mathrm{a_3}}\right)} \tag{7.2}$$

where the coefficients $\mathrm{a_1}$, $\mathrm{a_3}$, and $\mathrm{a_3}$ are to be determined numerically [104]. The

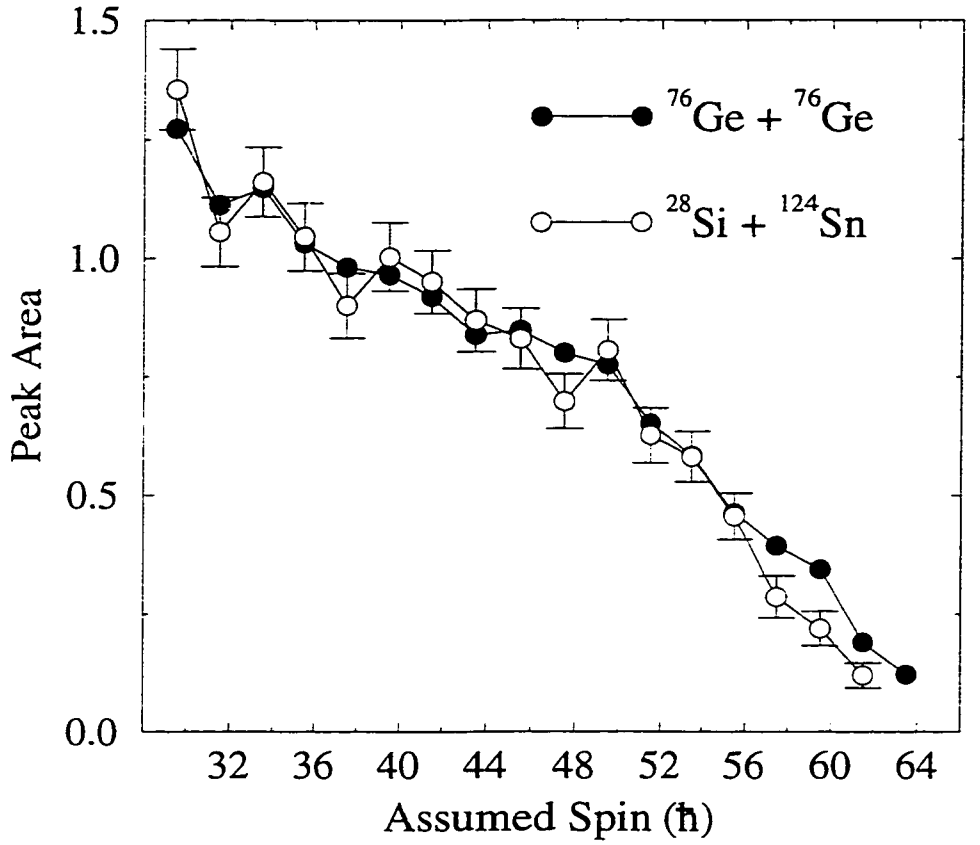

Figure 7.3: Peak-area profiles measured for the yrast superdeformed band in ^{147}Gd. Note that the error bars for the ^{76}Ge-induced reaction are no larger than the points plotted and have therefore been omitted for clarity.

Woods-Saxon function is ideal for extracting true intensity profiles of superdeformed bands since it has characteristics which resemble a feeding region and a "plateau" region, see figure 7.5. The result of the fit, normalized to one at the lowest spin, is shown in figure 7.6 for each reaction. Also shown are the error bands associated with the true relative intensity profile for the ^{28}Si-induced reaction. It is immediately evident that, within uncertainty, the a_2 and a_3 coefficients are equivalent for the two reactions studied. It should be pointed out that the actual value of the a_1 coefficient carries no physical significance and that it is merely related to the number of counts in the relevant spectrum. As a check, the profiles shown in figure 7.6 were substituted back into equation (7.1) to give the fitted forms shown in figure 7.4; the fits appear to be exceptional. The similarity of the two true intensity profiles, even at high spin, indicates that extra feeding of the superdeformed band in the mass-symmetric reaction occurs not only at the top of the band, as one might expect, but also continues through to the lower spins. Further investigation was therefore prompted in an attempt to determine the origin of the extra feeding measured for the mass-symmetric reaction.

A study of the superdeformed continuum feeding the yrast superdeformed states was undertaken. Gamma-gamma correlation arrays were constructed by double gating on the yrast superdeformed band in ^{147}Gd. Gates were only set on the bottom nine transitions (the plateau) of the band to ensure that all of the intensity of the continuum feeding the band would be measured and elliptical gates were used with the "spike-free" method of matrix incrementation. The resulting γ-γ matrix for the ^{76}Ge-induced reaction is shown in figure 7.7. A similar matrix was constructed for the ^{28}Si-induced reaction.

The operator method of reference [101] was extended such that background

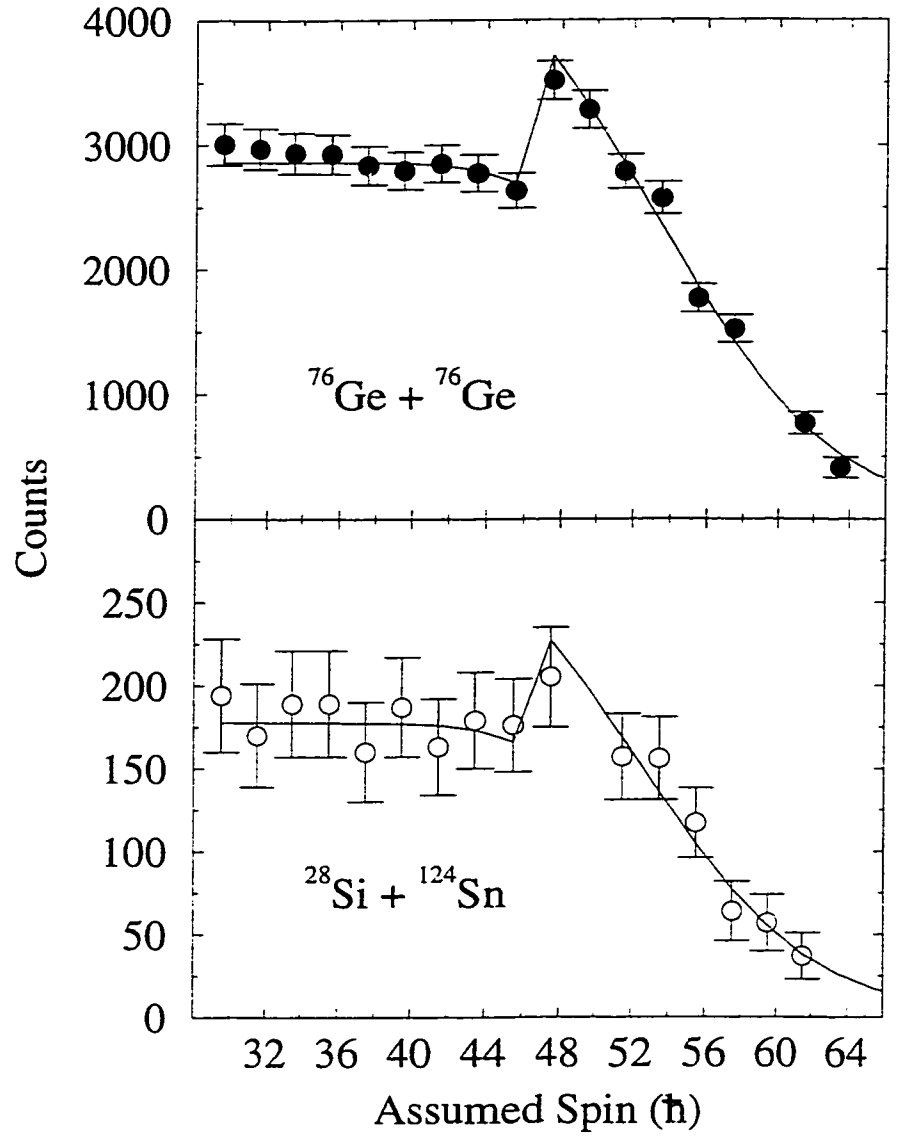

Figure 7.4: Efficiency-corrected peak-area profiles obtained by gating on the plateau (the bottom nine transitions) of the superdeformed band in ^{147}Gd. Experimental data points are shown as circles and the solid lines represent fits to these points.

subtraction of the γ-γ matrices could be performed. The resulting background-subtracted symmetrized matrices for the ^{76}Ge-induced and ^{28}Si-induced reactions are shown in figures 7.8 and 7.9, respectively. One immediately recognizes the regular two-dimensional representation of the superdeformed band. The dark clusters are

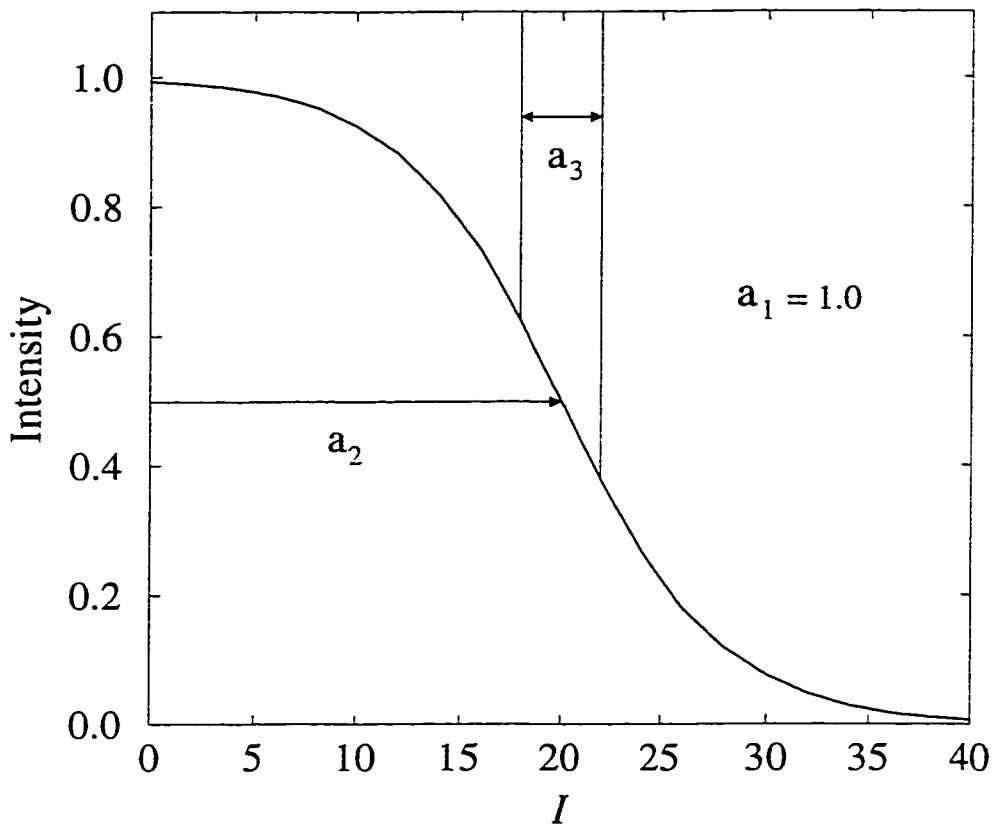

Figure 7.5: The Woods-Saxon function and its defining coefficients.

two-dimensional gaussians that correspond to γ-ray transitions of the superdeformed band. Also recognizable, for the mass-symmetric reaction, is the superdeformed continuum ridge that is in coincidence with the yrast superdeformed band in ^{147}Gd. The continuum ridge can be seen as a faint haze running along the first off-diagonal yrast superdeformed band transitions. A quantitative study of the ridge was undertaken as shall now be described.

The spectra shown in figures 7.10 and 7.11 were obtained by summing 27 keV wide slices taken perpendicular to and projected along the $E_{\gamma_1} = E_{\gamma_2}$ diagonal. These slices were made in two energy regions, namely, 997 keV $\leq (E_{\gamma_1} + E_{\gamma_2})/2 <$ 1241 keV and 1265 keV $\leq (E_{\gamma_1} + E_{\gamma_2})/2 <$ 1585 keV. In the first energy region, windows centered

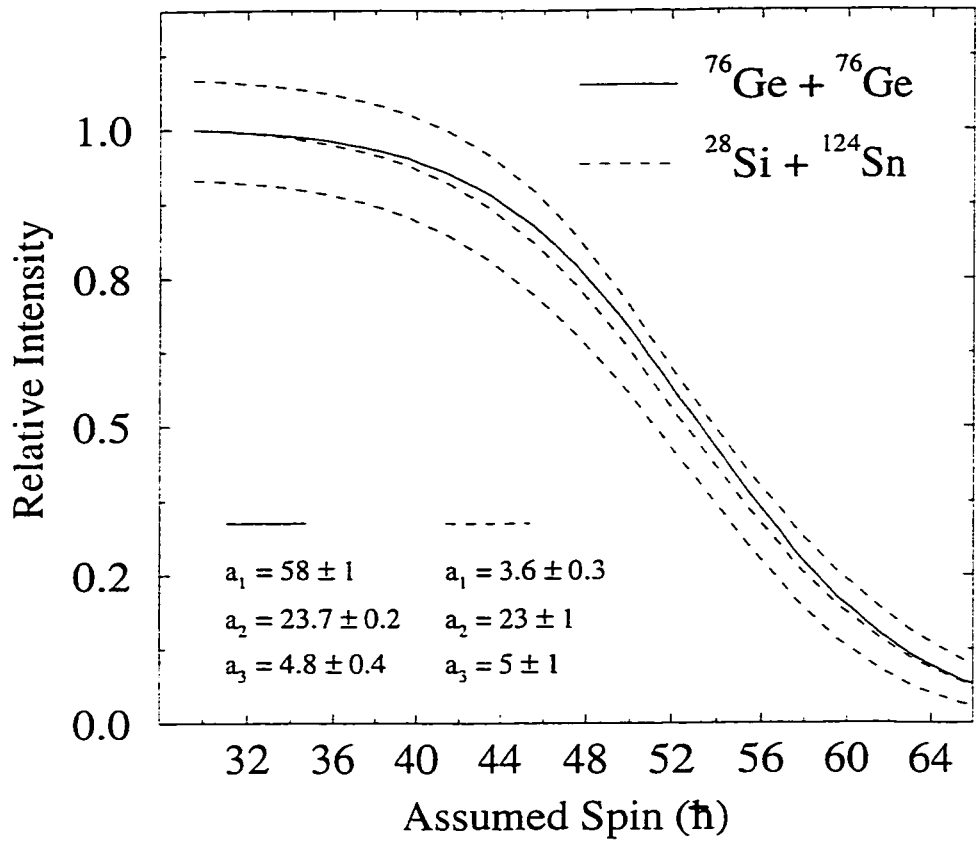

Figure 7.6: True relative intensity, $\mathcal{I}_t(I)$, profiles for the ^{76}Ge-induced and ^{28}Si-induced reactions. Each curve was normalized to one at the lowest assumed spin, the values listed for the a_1 coefficient correspond to values before normalization was performed. Also shown are the error bands associated with the ^{28}Si-induced reaction. It should be noted that a_1 is unitless and that a_2 and a_3 have units of $\hbar$.

around 1010, 1065, 1121, 1175, and 1228 keV were summed together. The resulting spectra are shown in figure 7.10 for the ^{76}Ge-induced reaction (upper panel) and for the ^{28}Si-induced reaction (lower panel). In the second energy region, windows centered around 1278, 1323, 1368, 1414, 1464, 1517, and 1571 keV were summed together. The resulting spectra are shown in figure 7.11 for the ^{76}Ge-induced reaction (upper panel) and for the ^{28}Si-induced reaction (lower panel). By following this procedure the first off-diagonal yrast superdeformed band transitions were avoided (see figure 7.8 for a clear visualization of this) and a study of the first superdeformed continuum ridge

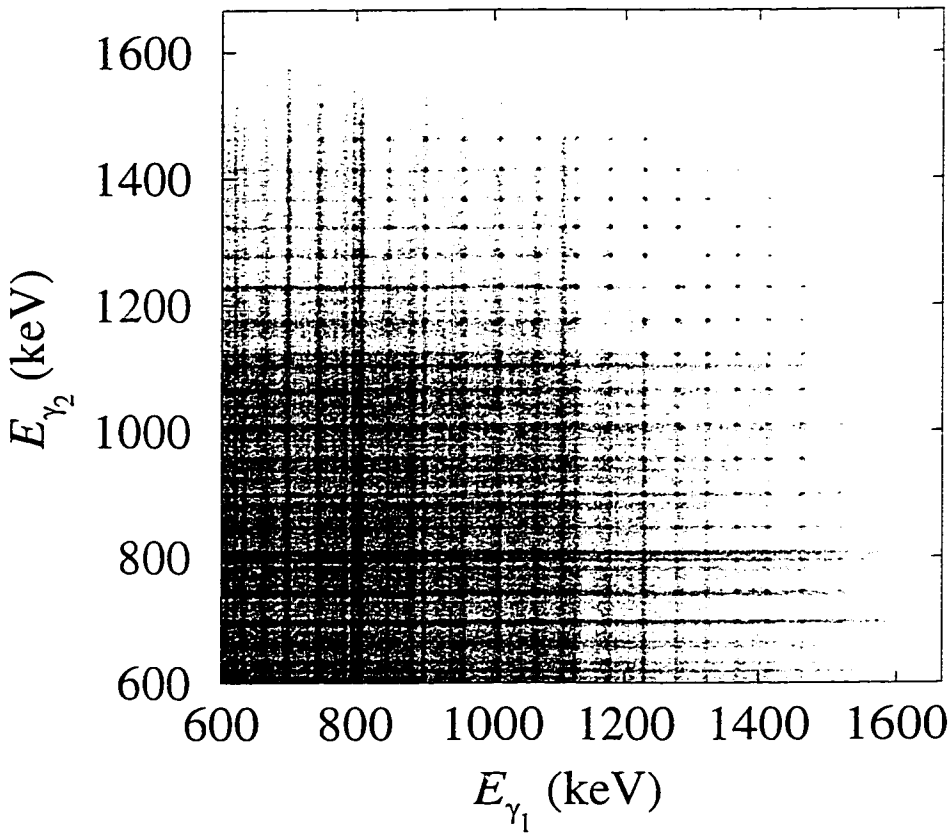

Figure 7.7: Portion of the doubly-gated γ-γ matrix for the yrast superdeformed band in ^{147}Gd, for the ^{76}Ge-induced reaction, obtained by setting gates on the bottom nine transitions of the band.

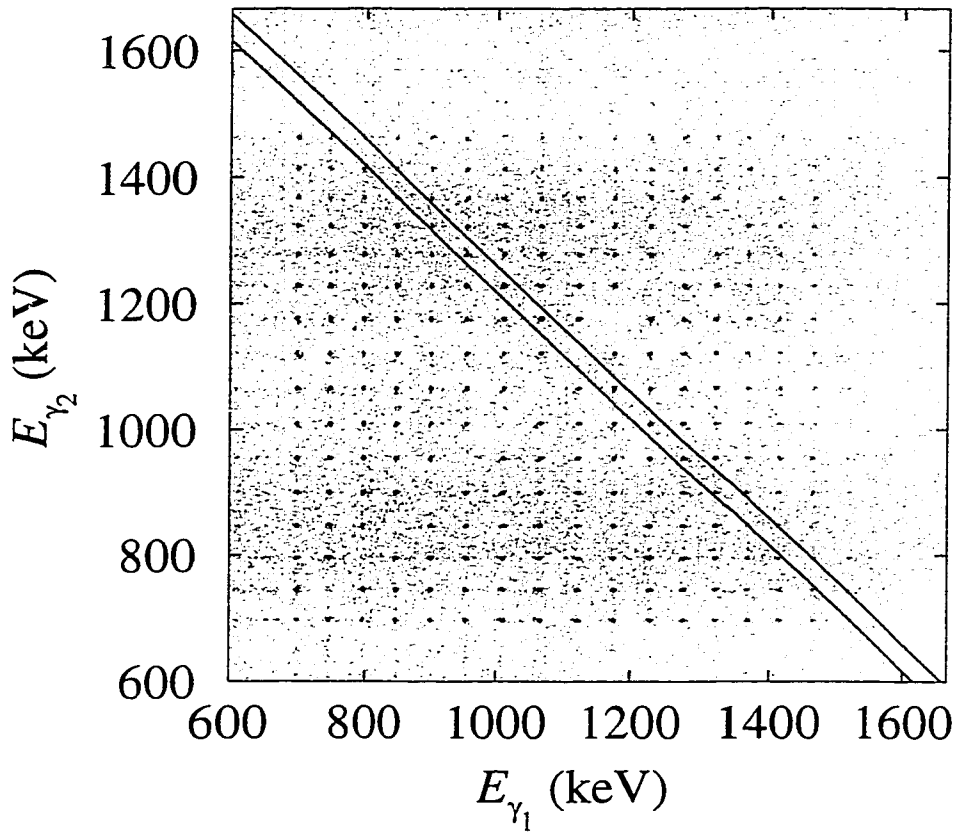

Figure 7.8: Portion of the doubly-gated background-subtracted γ-γ matrix for the yrast superdeformed band in ^{147}Gd, for the ^{76}Ge-induced reaction, obtained by setting gates on the bottom nine transitions of the band. The solid lines perpendicular to the $E_{\gamma_1} = E_{\gamma_2}$ diagonal illustrate how slices where chosen in order to avoid the first off-diagonal yrast superdeformed band transitions in the ridge analysis.

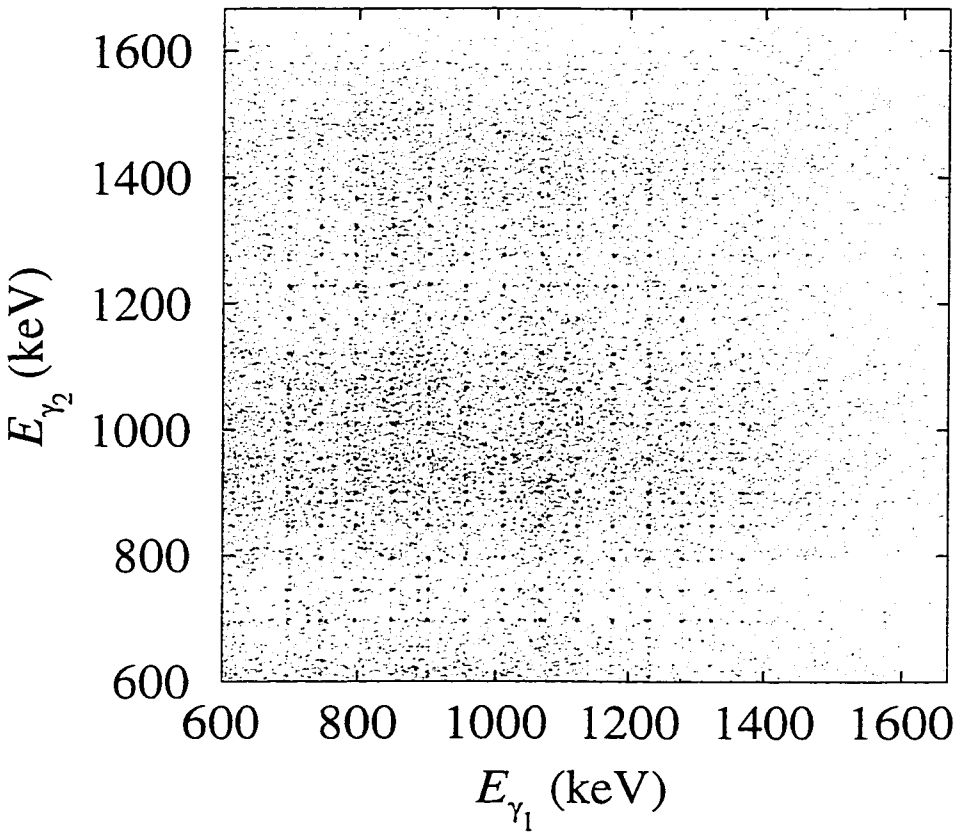

Figure 7.9: Portion of the doubly-gated background-subtracted γ-γ matrix for the yrast superdeformed band in ^{147}Gd, for the ^{28}Si-induced reaction, obtained by setting gates on the bottom nine transitions of the band.

could be done. If this technique were not employed then the slices made would be dominated by the yrast peaks at the position where the continuum is expected and a ridge analysis would have been extremely difficult. The second, fourth, sixth, etc. off-diagonal yrast peaks are of course still seen in figures 7.10 and 7.11 and correspond to the largest peaks.

As is evident from figures 7.10 and 7.11 no statistically significant continuum could be seen for the mass-asymmetric reaction, however, a clear view of the first ridge, determined to be 55 keV from the diagonal, was obtained for the mass-symmetric reaction. The intensity of this ridge over the two energy regions specified above was measured (taking into account the fact that not all channels were summed over) and compared to measured intensities of γ-γ coincidences occurring in the plateau region. A lower limit of 2.5 was placed on the intensity ratio of the superdeformed continuum (in the first ridge), relative to the yrast superdeformed band in ^{147}Gd, for the mass-symmetric reaction relative to the mass-asymmetric reaction. In other words, the superdeformed continuum feeding the yrast superdeformed band is at least $4.6 \times 2.5 \sim 12$ times as intense in that reaction (relative to normally deformed states) as compared to the mass-asymmetric reaction. It is therefore clear that, for the mass-symmetric reaction, at least part of the extra feeding of the superdeformed yrast states is associated with an increase in the superdeformed continuum. Thus, cascades feeding the discrete superdeformed band probably originate from a higher average entry point in the mass-symmetric reaction. Also, the large continuum intensity feeding the yrast superdeformed band in the mass-symmetric reaction could partially explain why the intensity profiles are nearly identical for both reactions. It should be pointed out that the ridge was not seen at high energy, as would be expected for continuum at extremely high spin, perhaps suggesting that the width of the ridge

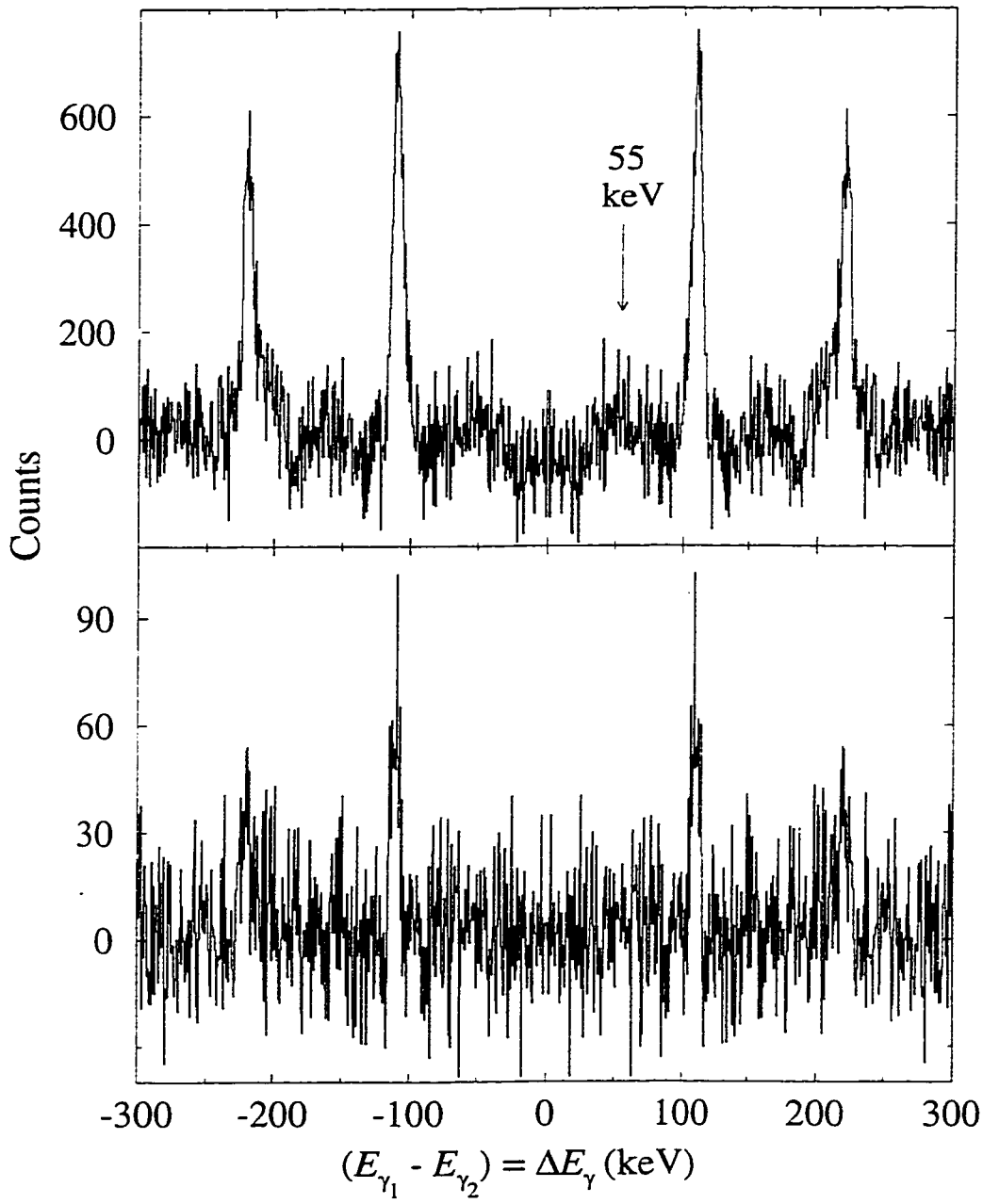

Figure 7.10: Sum of projections of the background-subtracted γ-γ matrices shown in figures 7.8 and 7.9. Projections were made along the $E_{\gamma_1} = E_{\gamma_2}$ diagonal in the energy range 997 keV $\leq (E_{\gamma_1} + E_{\gamma_2})/2 <$ 1241 keV. Upper panel: sum of projections for the mass-symmetric reaction. The arrow represents the centroid of the ridge, measured to be 55 keV from the diagonal. Lower panel: sum of projections for the mass-asymmetric reaction.

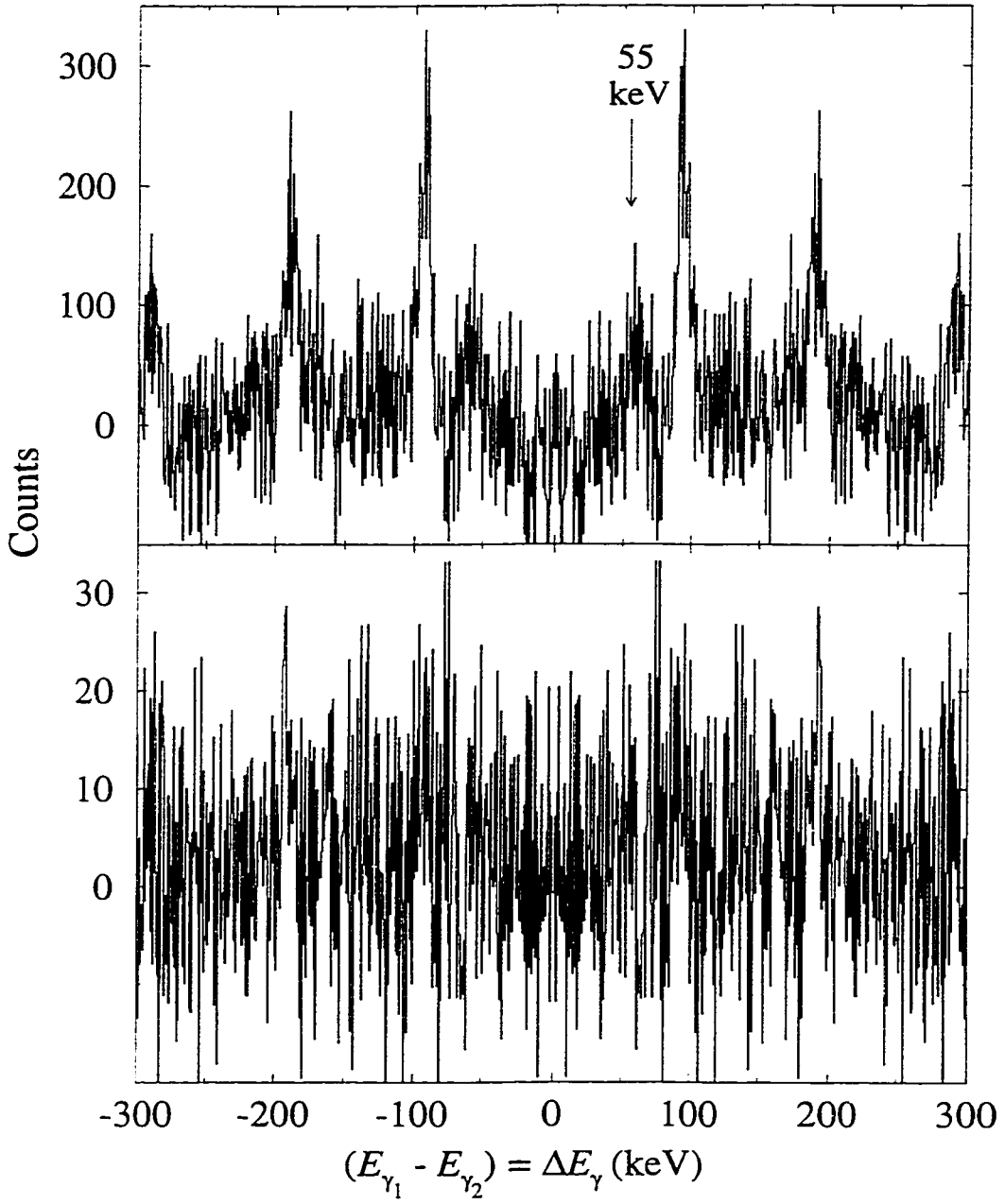

Figure 7.11: Sum of projections of the background-subtracted γ-γ matrices shown in figures 7.8 and 7.9. Projections were made along the $E_{\gamma_1} = E_{\gamma_2}$ diagonal in the energy range 1265 keV $\leq (E_{\gamma_1} + E_{\gamma_2})/2 <$ 1585 keV. Upper panel: sum of projections for the mass-symmetric reaction. The arrow represents the centroid of the ridge, measured to be 55 keV from the diagonal. Lower panel: sum of projections for the mass-asymmetric reaction.

increases with increasing energy. Reliable measurements to confirm this could of course not be made.

7.4 Summary

A study of superdeformed band population at very high angular momenta was undertaken with the reactions ^{76}Ge+^{76}Ge at 323 MeV and ^{28}Si+^{124}Sn at 152 MeV. Both reactions formed the compound nucleus ^{152}Gd at an excitation energy of 87 MeV. Relative to normally deformed states, the superdeformed band in the residual nucleus ^{147}Gd was found to be populated 4.6$\pm$0.2 times more strongly for the mass-symmetric reaction compared to the mass-asymmetric reaction. Such a large difference in the population was not expected and prompted further investigation. Intensity profiles indicated that, for the mass-symmetric reaction, the extra feeding occurs down the entire band and not just at the top of the band; one might expect extra feeding at the top of the band if the population difference observed for the two reactions was simply due to differences in their spin distributions. This result led to a study of the superdeformed continuum, in coincidence with the yrast superdeformed band in ^{147}Gd, in an attempt to determine the origin of the extra feeding. It was determined that the superdeformed continuum feeding the yrast superdeformed states in ^{147}Gd was at least 12 times stronger for the ^{76}Ge-induced reaction.

Dissipative collision calculations performed with the code HICOL suggest that the fusion time for the mass-symmetric reaction is about 6 times longer than that of the mass-asymmetric reaction; these calculations were carried out at the average spin of each compound-nucleus spin distribution. However, "time-dependent" statistical-model calculations of similar systems [105] suggest that an increased fusion time of even this amount may still not be long enough to explain the results of the present

study. One remaining concern is that perhaps the fission barrier used in theoretical calculations is not known well enough to understand what is happening at very high spins. If this is the case then experiments such as the one presented in this chapter are most likely the best means of learning more about the probability of surviving fission at extreme angular momenta.

Chapter 8

Conclusion

"But why shall I say more? ...
To-morrow I shall be fetterless!"

Edgar Allan Poe (1809-1849)
The Imp of the Perverse [106]

The main goal of this Thesis was to utilize the phenomenon of superdeformation as a "tool" to study fusion-evaporation reactions. In particular, ambiguities in existing interpretations of the processes governing fusion-evaporation reactions in the mass $A \sim 150$ region were scrutinized. Alternative explanations for measured increases in the population of superdeformed structures formed with mass-symmetric reactions compared to mass-asymmetric reactions were sought.

The idea of using superdeformation as a means of examining properties of fusion-evaporation reactions was first realized in a study that dealt with population enhancement of superdeformed states in ^{135}Nd. The compound nucleus ^{138}Nd was formed with the reactions ^{74}Ge+^{64}Ni and ^{26}Mg+^{112}Cd at bombarding energies of 239 and 94 MeV, respectively, ensuring that the excitation energies and uncoupled spin distributions of the reactions were properly matched. Coupled-channel calculations predicted dramatic increases in the population of high-spin states for the

mass-symmetric reaction compared to the mass-asymmetric reaction. Experimental measurements of normally deformed states in ^{134}Nd, ^{135}Nd, and ^{136}Nd and superdeformed states in ^{135}Nd proved these predictions to be true and so-called entrance channel effects were ruled out as a interpretation of the results. Statistical-model evaporation calculations were able to nicely reproduce the experimental results. Although the study dealt with nuclei in the mass $A \sim 130$ region, at spins for which the fission of compound nuclei is negligible, the coupled-channel effects could also play a major role in the mass $A \sim 150$ region. The primary difference in the mass $A \sim 150$ region is that one has to properly account for the competition between fission and particle evaporation.

A study of superdeformed band population in the mass $A \sim 150$ region was undertaken with the reactions ^{76}Ge+^{76}Ge and ^{28}Si+^{124}Sn at bombarding energies of 323 and 152 MeV, respectively. Coupled-channel calculations of spin distributions showed large increases in the population of high-spin states for the mass-symmetric reaction when compared to the mass-asymmetric reaction. However, statistical-model evaporation calculations predicted similar entry-spin distributions for the two reactions due to the fact that the compound nucleus ^{152}Gd formed in the mass-symmetric reaction losses much of its extra spin to fission. Thus, minimal differences in the population of superdeformed bands in the gadolinium isotopes were expected. Surprisingly, experimental measurements of the intensity of the yrast superdeformed band in ^{147}Gd showed a very large increase for the mass-symmetric reaction. Even more surprising was the fact that the intensity profile of that superdeformed band was independent of the reaction used. This discovery prompted a study of the continuum ridge feeding the yrast superdeformed band in ^{147}Gd. The presence of a continuum ridge measured in the mass-symmetric reaction and the apparent lack of one in the mass-asymmetric

reaction suggested that at least part of the extra feeding of the superdeformed yrast states measured in the mass-symmetric reaction is associated with an increase in the superdeformed continuum. A complete explanation for the origin of the extra feeding is, however, still lacking and further investigation is needed.

Perhaps one of the most important ingredients missing from many of the evaporation codes available is the inclusion of time dependence in the fusion and fission processes. Codes like evapOR can be modified such that time dependence is mimicked (see for example reference [105]) but the manner in which this is done is arguable. The combination of true time-dependent evaporation codes along with coupled-channel calculations may be what is needed in the modelling of experimental results like those presented in this Thesis. Furthermore, it is possible that the fission barrier used in theoretical calculations is not known well enough to understand what is happening to nuclei that are produced at very high angular momenta.

In an upcoming experiment [107] the compound nucleus ^{190}Hg will be produced at an excitation energy of 38 MeV via the reactions ^{80}Se + ^{110}Pd and ^{48}Ca + ^{142}Nd at bombarding energies around their Coulomb barriers. Calculations predict that these two reactions should populate identical compound-nucleus spin distributions when coupling to inelastic channels are not taken into account. However, coupled-channel calculations predict large differences in these spin distributions and even when fission of ^{190}Hg is taken into account measurable differences in the population of high-spin states are expected. In other words, for the upcoming experiment, fission is not expected to affect the compound-nucleus spin distributions as drastically as it did, for example, in the mass $A \sim 150$ region study presented in this Thesis. Differences in spin distributions will be measured experimentally by studying the population of discrete states in the evaporation residues and the γ-ray multiplicities

with the 8π Spectrometer. The data collected will hopefully provide further tests for existing fusion and fission models.

Bibliography

[1] The Beatles. *Get Back, Let It Be.* EMI Records Ltd., 1970.

[2] J. M. Nieminen, S. Flibotte, A. Galindo-Uribarri, G. Viesti, G. C. Ball, D. Bazzacco, M. Cromaz, G. de Angelis, J. De Graaf, M. De Poli, T. E. Drake, D. Fabris, Ch. Finck, V. P. Janzen, S. Lunardi, M. Lunardon, N. H. Medina, G. Maron, C. M. Petrache, D. C. Radford, C. Rossi-Alvarez, O. Stezowski, Ch. Theisen, J. C. Waddington, D. Ward, and J. N. Wilson. *Physical Review C*, 54:2764, 1996.

[3] J. M. Nieminen, S. Flibotte, M. Cromaz, A. Galindo-Uribarri, G. Gervais, D. S. Haslip, V. P. Janzen, D. C. Radford, C. E. Svensson, J. C. Waddington, D. Ward, and J. N. Wilson. *Physical Review Letters*, 78:3832, 1997.

[4] J. M. Nieminen, S. Flibotte, G. Gervais, D. S. Haslip, I. Y. Lee, A. O. Macchiavelli, R. W. MacLeod, O. Stezowski, C. E. Svensson, J. C. Waddington, and J. N. Wilson. *Physical Review C*, in press, 1998.

[5] *The Norton Anthology of American Literature*, volume 1. W. W. Norton & Company, New York, second edition, 1985.

[6] S. M. Polikanov, V. A. Druin, V. A. Karnaukhov, V. L. Mikheev, A. A. Pleve, N. K. Skobelev, V. G. Subbotin, G. M. Ter-Akop'Yan, and V. A. Fomichev. *Soviet Physics JETP*, 15:1016, 1962.

[7] P. J. Nolan, A. Kirwan, D. J. G. Love, A. H. Nelson, D. J. Unwin, and P. J. Twin. *Journal of Physics G*, 11:L17, 1985.

[8] P. J. Twin, B. M. Nyakó, A. H. Nelson, J. Simpson, M. A. Bentley, H. W. Cranmer-Gordon, P. D. Forsyth, D. Howe, A. R. Mokhtar, J. D. Morrison, J. F. Sharpey-Schafer, and G. Sletten. *Physical Review Letters*, 57:811, 1986.

[9] E. F. Moore, R. V. F. Janssens, R. R. Chasman, I. Ahmad, T. L. Khoo, F. L. H. Wolfs, D. Ye, K. B. Beard, U. Garg, M. W. Drigert, Ph. Benet, Z. W. Grabowski, and J. A. Cizewski. *Physical Review Letters*, 63:360, 1989.

[10] C. Baktash, D. M. Cullen, J. D. Garrett, C. J. Gross, N. R. Johnson, W. Nazarewicz, D. G. Sarantites, J. Simpson, and T. R. Werner. *Physical Review Letters*, 74:1946, 1995.

[11] C. E. Svensson, C. Baktash, J. A. Cameron, M. Devlin, J. Eberth, S. Flibotte, D. S. Haslip, D. R. LaFosse, I. Y. Lee, A. O. Macchiavelli, R. W. MacLeod, J. M. Nieminen, S. D. Paul, L. L. Riedinger, D. Rudolph, D. G. Sarantites, H. G. Thomas, J. C. Waddington, W. Weintraub, J. N. Wilson, A. V. Afanasjev, and I. Ragnarsson. *Physical Review Letters*, 79:1233, 1997.

[12] B. Singh, R. B. Firestone, and S. Y. F. Chu. *Table of Superdeformed Nuclear Bands and Fission Isomers.* Lawrence Berkeley National Laboratory, Berkeley, second edition, 1996.

[13] R. P. Feynman. *QED, The Strange Theory of Light and Matter.* Princeton University Press, New Jersey, 1985.

[14] D. L. Hill and J. A. Wheeler. *Physical Review*, 89:1102, 1953.

[15] H. Ejiri and M. de Voigt. *Gamma-Ray and Electron Spectroscopy in Nuclear Physics.* Oxford, New York, 1989.

[16] A. Bohr and B. Mottelson. *Nuclear Structure*, volume 2. Benjamin, New York, 1975.

[17] G. Hackman. PhD thesis, McMaster University, 1995.

[18] S. Nilsson. *Mat. Fys. Medd. Dan. Vid. Selsk.*, 29, 1955.

[19] C. M. Lederer and V. S. Shirley, editors. *Table of Isotopes.* John Wiley & Sons, New York, seventh edition, 1978.

[20] D. R. Inglis. *Physical Review*, 96:1059, 1954.

[21] W. Nazarewicz, R. A. Wyss, and A. Johnson. *Nuclear Physics*, A503:285, 1989.

[22] R. Kostelanetz, editor. *John Cage: An Anthology.* Da Capo Press, New York, 1991.

[23] N. Bohr. *Nature*, 137:344, 1936.

[24] R. M. Diamond and F. S. Stephens. *Annual Review of Nuclear and Particle Science*, 30:85, 1980.

[25] D. L. Hillis, J. D. Garrett, O. Christensen, B. Fernandez, G. B. Hagemann, B. Herskind, B. B. Back, and F. Folkman. *Nuclear Physics*, A325:216, 1979.

[26] G. Gervais. Master's thesis, McMaster University, 1997.

[27] G. F. Knoll. *Radiation Detection and Measurement.* John Wiley & Sons, New York, second edition, 1989.

[28] H. R. Andrews *et al. Proposal for a National Facility - The* 8π *Spectrometer.* AECL-8329, Chalk River Laboratories, 1984.

[29] J. P. Martin, D. C. Radford, M. Beaulieu, P. Taras, D. Ward, H. R. Andrews, G. Ayotte, F. J. Sharp, J. C. Waddington, O. Häusser, and J. Gascon. *Nuclear Instruments and Methods in Physics Research A*, 257:301, 1987.

[30] T. E. Drake, J. C. Waddington, H. R. Andrews, D. C. Radford, and D. and Ward. *Proposal for a National Facility - The TRIGAM Spectrometer.* 1992.

[31] I. Y. Lee. *Nuclear Physics*, A520:641c, 1990.

[32] D. Bazzacco. In *Proceedings of the International Conference on Nuclear Structure at High Angular Momentum*, page 376, Ottawa, 1992. AECL-10613.

[33] E. Farnea, G. de Angelis, A. Buscemi, R. Zanon, R. Isocrate, M. De Poli, D. Bazzacco, P. Pavan, P. Spolaore, Y. Li, D. Napoli, S. Lunardi, C. Rossi-Alvarez, A. M. Bizzeti-Sona, and P. G. Bizzeti. *Istituto Nazionale di Fisica Nucleare Laboratori Nazionali di Legnaro, Annual Report*, page 189, 1994.

[34] L. J. Peter. *Quotations for our time.* William Morrow & Company, U.S.A., 1977.

[35] W. Nörenberg. *Heavy Ion Collisions*, volume 2. North-Holland, Amsterdam, 1980.

[36] W. J. Swiatecki. *Physica Scripta*, 24:113, 1981.

[37] H. Feldmeier. *Reports on Progress in Physics*, 50:915, 1987.

[38] M. Thoennessen and J. R. Beene. *Physics Review C*, 45:873, 1992.

[39] H. Feldmeier. *Computer code HICOL*, 1986.

[40] W. Reisdorf, F. P. Hessberger, K. D. Hildenbrand, S. Hofmann, G. Müzenberg, K. H. Schmidt, J. H. R. Schneider, W. F. W. Schneider, K. Sümmerer, G. Wirth, J. V. Kratz, and K. Schlitt. *Physical Review Letters*, 49:1811, 1982.

[41] R. Vandenbosch. *Annual Review of Nuclear and Particle Science*, 42:447, 1992.

[42] C. H. Dasso and S. Landowne. *Computer Physics Communications*, 46:187, 1987.

[43] C. H. Dasso, S. Landowne, and A. Winther. *Nuclear Physics*, A405:381, 1983.

[44] C. H. Dasso, S. Landowne, and A. Winther. *Nuclear Physics*, A407:221, 1983.

[45] R. A. Broglia, C. H. Dasso, S. Landowne, and G. Pollarolo. *Physics Letters*, 133B:34, 1983.

[46] S. Landowne and C. H. Dasso. *Physics Letters*, 138B:32, 1984.

[47] P. R. Christensen and A. Winther. *Physics Letters*, 65B:19, 1976.

[48] P. H. Stelson and L. Grodzins. *Nuclear Data A*, 1:21, 1965.

[49] R. H. Spear. *Atomic Data and Nuclear Data Tables*, 42:55, 1989.

[50] N. G. Nicolis, D. G. Sarantites, and J. R. Beene. *Computer code evapOR, unpublished.*

[51] A. Gavron. *Physical Review C*, 21:230, 1980.

[52] F. Pühlhofer. *Nuclear Physics*, A280:267, 1977.

[53] R. Bass. *Physics Letters*, 47B:139, 1973.

[54] J. M. Blatt and V. F. Weisskopf. *Theoretical Nuclear Physics.* John Wiley & Sons, New York, 1952.

[55] A. Gilbert and A. G. W. Cameron. *Canadian Journal of Physics*, 43:1446, 1965.

[56] J. L. Egido and P. Ring. *Journal of Physics G*, 19:1, 1993.

[57] J. Bartlett. *Bartlett's Familiar Quotations.* Little, Brown and Company, Toronto, 1968.

[58] B. Haas, V. P. Janzen, D. Ward, H. R. Andrews, D. C. Radford, D. Prévost, J. A. Kuehner, A. Omar, J. C. Waddington, T. E. Drake, A. Galindo-Uribarri, G. Zwartz, S. Flibotte, P. Taras, and I. Ragnarsson. *Nuclear Physics*, A561:251, 1993.

[59] S. M. Mullins, N. C. Schmeing, S. Flibotte, G. Hackman, J. L. Rodriguez, J. C. Waddington, L. Yao, H. R. Andrews, A. Galindo-Uribarri, V. P. Janzen, D. C. Radford, D. Ward, J. De Graaf, T. E. Drake, S. Pilotte, and E. S. Paul. *Physical Review C*, 50:R2261, 1994.

[60] B. Haas, D. Ward, H. R. Andrews, G. C. Ball, T. E. Drake, S. Flibotte, A. Galindo-Uribarri, V. P. Janzen, J. K. Johansson, H. Kluge, J. A. Kuehner, A. Omar, S. Pilotte, D. Prévost, J. L. Rodriguez, D. C. Radford, P. Taras, J. P. Vivien, J. C. Waddington, and S. Aberg. *Physical Review C*, 42:R1817, 1990.

[61] D. Curien, G. de France, C. W. Beausang, F. A. Beck, T. Byrski, S. Clarke, P. Dagnall, G. Duchêne, S. Flibotte, S. Forbes, P. D. Forsyth, B. Haas, M. A. Joyce, B. Kharraja, B. M. Nyakó, C. Schück, J. Simpson, Ch. Theisen, P. J. Twin, J. P. Vivien, and L. Zolnai. *Physical Review Letters*, 71:2559, 1993.

[62] D. S. Haslip, G. Hackman, and J. C. Waddington. *Nuclear Instruments and Methods in Physics Research A*, 345:534, 1994.

[63] D. C. Radford. *Nuclear Instruments and Methods in Physics Research A*, 361:297, 1995.

[64] A. Ataç, M. Piiparinen, B. Herskind, J. Nyberg, G. Sletten, G. de Angelis, S. Forbes, N. Gjørup, G. Hagemann, F. Ingebretsen, H. Jensen, D. Jerrestam, H. Kusakari, R. M. Lieder, G. V. Marti, S. M. Mullins, D. Santonocito, H. Schnare, K. Strähle, M. Sugawara, P. O. Tjøm, A. Virtanen, and R. Wadsworth. *Physical Review Letters*, 70:1069, 1993.

[65] K. Zuber, D. Balouka, F. A. Beck, Th. Byrski, D. Curien, G. de France, G. Duchêne, C. Gehringer, B. Haas, J. C. Merdinger, P. Romain, D. Santos, J. Styczen, J. P. Vivien, J. Dudek, Z. Szymański, and T. R. Werner. *Physics Letters*, 254B:308, 1991.

[66] C. Schumacher, O. Stuch, T. Rzaça-Urban, P. von Brentano, A. Dewald, A. Georgiev, R. Lieder, F. Linden, J. Lisle, J. Theuerkauf, W. Urban, S. Utzelmann, and D. Weißhaar. *Physical Review C*, 52:1302, 1995.

[67] P. Taras, S. Flibotte, J. Gascon, B. Haas, S. Pilotte, D. C. Radford, D. Ward, H. R. Andrews, G. C. Ball, F. Banville, S. Cournoyer, D. Horn, J. K. Johansson, S. Monaro, N. Nadon, D. Prévost, C. Pruneau, D. Thibault, D. M. Tucker, and J. C. Waddington. *Physical Review Letters*, 61:1348, 1988.

[68] C. Schumacher, P. von Brentano, A. Dewald, M. Eschenauer, H. Grawe, J. Heese, K. H. Maier, M. Philipp, E. Radermacher, R. Schubart, O. Stuch,

J. Theuerkauf, D. Weißhaar, and M. Wilhelm. *Zeitschrift für Physik A*, 351:39, 1995.

[69] G. Smith, B. Haas, A. Alderson, I. Ali, C. W. Beausang, M. A. Bentley, P. Dagnall, P. Fallon, G. de France, P. D. Forsyth, U. Huttmeier, P. Romain, D. Santos, P. J. Twin, and J. P. Vivien. *Physical Review Letters*, 68:158, 1992.

[70] S. Flibotte, H. R. Andrews, T. E. Drake, A. Galindo-Uribarri, B. Haas, V. P. Janzen, D. Prévost, D. C. Radford, J. L. Rodriguez, P. Romain, J. P. Vivien, J. C. Waddington, D. Ward, and G. Zwartz. *Physical Review C*, 45:R889, 1992.

[71] L. H. Zhu, M. Cinausero, S. Lunardi, G. Viesti, D. Bazzacco, G. de Angelis, M. De Poli, D. Fabris, E. Fioretto, A. Gadea, F. Lucarelli, N. H. Medina, D. R. Napoli, C. M. Petrache, G. Prete, and C. Rossi-Alvarez. *Istituto Nazionale di Fisica Nucleare Laboratori Nazionali di Legnaro, Annual Report*, page 58, 1995.

[72] L. H. Zhu, M. Cinausero, S. Lunardi, G. Viesti, D. Bazzacco, G. de Angelis, M. De Poli, D. Fabris, E. Fioretto, A. Gadea, F. Lucarelli, M. Lunardon, N. H. Medina, D. R. Napoli, C. M. Petrache, G. Prete, and C. Rossi-Alvarez. *Istituto Nazionale di Fisica Nucleare Laboratori Nazionali di Legnaro, Annual Report*, page 83, 1996.

[73] S. Flibotte and J. M. Nieminen. *Journal of Physics G*, 23:1183, 1997.

[74] S. M. Mullins, J. Nyberg, A. Maj, M. S. Metcalfe, P. J. Nolan, P. H. Regan, R. Wadsworth, and R. A. Wyss. *Physics Letters*, 312B:272, 1993.

[75] G. Viesti, T. Negro, D. Bazzacco, R. Burch, G. de Angelis, M. De Poli, D. Fabris, E. Fioretto, S. Lunardi, G. Nebbia, G. Prete, J. Rico, and C. Rossi-Alvarez. *Nuclear Physics*, A579:225, 1994.

[76] T. Lauritsen *et al.* In *Proceedings of the International Conference on Nuclear Structure at High Angular Momentum*, page 59, Ottawa, 1992. AECL-10613.

[77] F. Soramel, T. L. Khoo, Ph. Benet, K. B. Beard, R. V. F. Janssens, I. Ahmad, I. Bearden, M. P. Carpenter, P. J. Daly, M. W. Drigert, B. Fornal, U. Garg, Z. Grabowski, T. Lauritsen, Y. Liang, R. Mayer, E. F. Moore, W. Reviol, and D. Ye. *Physics Letters*, 350B:173, 1995.

[78] S. Flibotte, M. Cromaz, J. De Graaf, T. E. Drake, A. Galindo-Uribarri, G. Hackman, V. P. Janzen, S. M. Mullins, D. C. Radford, J. C. Waddington, D. Ward, and J. N. Wilson. *Physical Review C*, 53:R533, 1996.

[79] W. Kühn, P. Chowdhury, R. V. F. Janssens, T. L. Khoo, F. Haas, J. Kasagi, and R. M. Ronningen. *Physical Review Letters*, 51:1858, 1983.

[80] R. V. F. Janssens, R. Holzmann, W. Henning, T. L. Khoo, K. T. Lesko, G. S. F. Stephans, D. C. Radford, A. M. Van Den Berg, W. Kühn, and R. M. Ronningen. *Physics Letters*, 181A:16, 1986.

[81] A. Ruckelshausen, R. D. Fischer, W. Kühn, V. Metag, R. Mühlhans, R. Novotny, T. L. Khoo, R. V. F. Janssens, H. Gröger, D. Habs, H. W. Heyng, R. Repnow, D. Schwalm, G. Duchêne, R. M. Freeman, B. Haas, F. Haas, S. Hlavac, and R. S. Simon. *Physical Review Letters*, 56:2356, 1986.

[82] N. Rowley, G. R. Satchler, and P. H Stelson. *Physics Letters*, 254B:25, 1991.

[83] W. Reisdorf and references therein. *Journal of Physics G*, 20:1297, 1994.

[84] B. Haas, G. Duchêne, F. A. Beck, T. Byrski, C. Gehringer, J. C. Merdinger, A. Nourredine, V. Rauch, J. P. Vivien, J. Barrette, S. Tobbeche, E. Bożek,

J. Styczen, J. Keinonen, J. Dudek, and W. Nazarewicz. *Physical Review Letters*, 54:398, 1985.

[85] D. J. G. Love, P. J. Bishop, A. Kirwan, P. J. Nolan, D. J. Thornley, A. H. Nelson, and P. J. Twin. *Physical Review Letters*, 57:551, 1986.

[86] J. L. Barreto, N. G. Nicolis, D. G. Sarantites, R. J. Charity, L. G. Sobotka, D. W. Stracener, D. C. Hensley, J. R. Beene, C. Baktash, M. Halbert, and M. Thoennessen. *Physical Review C*, 48:2881, 1993.

[87] R. Wadsworth, S. M. Mullins, J. R. Hughes, P. J. Nolan, A. Kirwan, P. J. Bishop, I. Jenkins, M. J. Godfrey, and D. J. Thornley. *Journal of Physics G*, 15:L47, 1989.

[88] E. M. Beck, F. S. Stephens, J. C. Bacelar, M. A. Deleplanque, R. M. Diamond, J. E. Draper, C. Duyar, and R. J. McDonald. *Physical Review Letters*, 58:2182, 1987.

[89] C. M. Petrache, D. Bazzacco, S. Lunardi, C. Rossi-Alvarez, R. Venturelli, D. Bucurescu, C. A. Ur, D. De Acuña, G. Maron, D. R. Napoli, N. H. Medina, J. R. B. Oliveira, and R. Wyss. *Physics Letters*, 373B:275, 1996.

[90] M. A. Deleplanque, S. Frauendorf, R. M. Clark, R. M. Diamond, F. S. Stephens, J. A. Becker, M. J. Brinkman, B. Cederwall, P. Fallon, L. P. Farris, E. A. Henry, H. Hubel, J. R. Hughes, W. Korten, I. Y. Lee, A. O. Macchiavelli, M. A. Stoyer, P. Willsau, J. E. Draper, C. Duyar, and E. Rubel. *Physical Review C*, 52:R2302, 1995.

[91] K. Schiffer, B. Herskind, and J. Gascon. *Zeitschrift für Physik A*, 332:17, 1989.

[92] T. L. Khoo, T. Lauritsen, I. Ahmad, M. P. Carpenter, P. B. Fernandez, R. V. F. Janssens, E. F. Moore, F. L. H. Wolfs, Ph. Benet, P. J. Daly, K. B. Beard, U. Garg, D. Ye, and M. W. Drigert. *Nuclear Physics*, A557:83c, 1993.

[93] A. Huxley. *Brave New World.* Grafton Books, London, 1977.

[94] A. J. Sierk. *Physical Review C*, 33:2039, 1986.

[95] M. A. Deleplanque, C. Beausang, J. Burde, R. M. Diamond, J. E. Draper, C. Duyar, A. O. Macchiavelli, R. J. McDonald, and F. S. and Stephens. *Physical Review Letters*, 60:1626, 1988.

[96] D. S. Haslip. *Private Communications.*

[97] C. W. Beausang, D. Prévost, M. H. Bergstrom, G. de France, B. Haas, J. C. Lisle, Ch. Theisen, J. Timár, P. J. Twin, and J. N. Wilson. *Nuclear Instruments and Methods in Physics Research A*, 364:560, 1995.

[98] B. Crowell, M. P. Carpenter, R. G. Henry, R. V. F. Janssens, T. L. Khoo, T. Lauritsen, and D. Nisius. *Nuclear Instruments and Methods in Physics Research A*, 355:575, 1995.

[99] D. S. Haslip, S. Flibotte, G. de France, M. Devlin, A. Galindo-Uribarri, G. Gervais, G. Hackman, D. R. LaFosse, I. Y. Lee, F. Lerma, A. O. Macchiavelli, R. W. MacLeod, S. M. Mullins, J. M. Nieminen, D. G. Sarantites, C. E. Svensson, J. C. Waddington, and J. N. Wilson. *Physical Review Letters*, 78:3447, 1997.

[100] J. N. Wilson, R. A. E. Austin, D. S. Haslip, and J. C. Waddington. *Nuclear Instruments and Methods in Physics Research A*, 399:147, 1997.

[101] G. Hackman and J. C. Waddington. *Nuclear Instruments and Methods in Physics Research A*, 357:559, 1995.

[102] Ch. Theisen, N. Khadiri, J. P. Vivien, I. Ragnarsson, C. W. Beausang, F. A. Beck, G. Belier, T. Byrski, D. Curien, G. de France, D. Disdier, G. Duchêne, Ch. Finck, S. Flibotte, B. Gall, B. Haas, H. Hanine, B. Herskind, B. Kharraja, J. C. Merdinger, A. Nourreddine, B. M. Nyakó, G. E. Perez, D. Prévost, O. Stezowski, V. Rauch, C. Rigollet, H. Savajols, J. F. Sharpey-Schafer, P. J. Twin, L. Wei, and K. Zuber. *Physical Review C*, 54:2910, 1996.

[103] O. Bakander, C. Baktash, J. Borggreen, J. B. Jensen, K. Kownacki, J. Pedersen, G. Sletten, D. Ward, H. R. Andrews, O. Häusser, P. Skensved, and P. Taras. *Nuclear Physics*, A389:93, 1982.

[104] P. R. Bevington and D. K. Robinson. *Data Reduction and Error Analysis for the Physical Sciences.* McGraw-Hill, New York, second edition, 1992.

[105] J. R. Beene. *Nuclear Physics*, A583:73, 1995.

[106] E. A. Poe. *Selected Tales.* Oxford University Press, Oxford, 1987.

[107] S. Flibotte, B. Schaly, D. S. Haslip, J. M. Nieminen, C. E. Svensson, J.C. Waddington, J. N. Wilson, S. Courtin, N. Rowley, and J. P. Vivien. *LBL proposal form for the 88 inch cyclotron*, 1997.